Pressure–Temperature Evolution of a Late Palaeozoic Paired Metamorphic Belt in North–Central Chile (34°–35°30′S)

ARNE P. WILLNER*

INSTITUT FÜR GEOLOGIE, MINERALOGIE & GEOPHYSIK, RUHR-UNIVERSITÄT, D-44780 BOCHUM, GERMANY

In the Chilean Coastal Cordillera, two units, the Western and Eastern Series, constitute coeval parts of a Late Palaeozoic paired metamorphic belt dominated by siliciclastic metasediments. The Western Series also contains rocks from the upper oceanic crust and represents an accretionary prism. Omnipresent high-pressure conditions are reflected by Na–Ca-amphibole and phengite in greenschists. Peak PT conditions of 7·0–9·3 kbar, 380–420°C point to a metamorphic gradient of 11–16°C/km. Three unique occurrences of blueschist yield deviating conditions of 9·5–10·7 kbar, 350–385°C and are interpreted as relics from the lowermost part of the basal accretion zone preserving the original gradient of 9–11°C/km along the subducting slab. Pervasive ductile deformation related to basal accretion occurred near peak PT conditions. Deformation and PT evolution of the metapsammopelitic rocks is similar to that of the metabasites. However, a rare garnet mica-schist yields peak PT conditions of 9·6–14·7 kbar, 390–440°C reflecting a retrograde stage after cooling from a high-temperature garnet-forming stage. It is considered to be an exhumed relic from the earliest siliciclastic rocks subducted below a still hot mantle wedge. A retrograde overprint of all rock types occurred at ∼300–380°C. Continuous reactions caused crystal growth and recrystallization with abundant free water mostly under strain-free conditions. They record a pressure release of 3–4 kbar without erasing peak metamorphic mineral compositions. The Eastern Series lacks metabasite intercalations and represents a less deformed retro-wedge area. In the study area it was entirely overprinted at a uniform depth at 3 ± 0·5 kbar with temperatures progressively rising from 400°C to 720°C towards the coeval Late Palaeozoic magmatic arc batholith. The interrelated pattern of PT data permits a conceptual reconstruction of the fossil convergent margin suggesting a flat subduction angle of ∼25° with continuous basal accretion at a depth of 25–40 km and a short main intrusion pulse in the magmatic arc. The latter was accompanied by the formation of a thermal dome in the retro-wedge area, which remained stable relative to the vertically growing accretionary prism characterized by cyclic mass flow.

INTRODUCTION

The basement of the Coastal Cordillera in central Chile between Pichilemu and Constitución (34°–35°30′S; Fig. 1) represents the first region on the South American active continental margin in which metamorphic zonation was studied (González Bonorino, 1971). This resulted in recognition of this area as a classic Pacific-rim type paired metamorphic belt (Aguirre et al., 1972; Ernst, 1975). Principles and concepts were recognized here that could be applied to most of the metamorphic basement along the Chilean Coastal Cordillera between 26° and 55°S (Hervé, 1988). This unusually long chain of basement exposures represents a series of fossil, deeply subducted accretionary prisms of Permo-Carboniferous age in the north and Mesozoic age in the south that are partly associated with magmatic arcs and high-temperature metamorphic belts of variable age (Hervé, 1988). The metamorphic complexes were not overprinted by later collisional processes, but were destroyed to variable extents by processes after the end of accretion during the continuing long-term activity at the convergent margin.

The type area was revisited because it exposes the most characteristic elements of the Chilean basement. Here we concentrate primarily on metamorphic processes and correlate these with concomitant deformation and magmatic events. Together with an associated geochronological study (Willner et al., 2005) this provides a basis for development of a more detailed conceptual dynamic model for this type of active continental margin. Questions addressed in detail are: What partial PT paths can
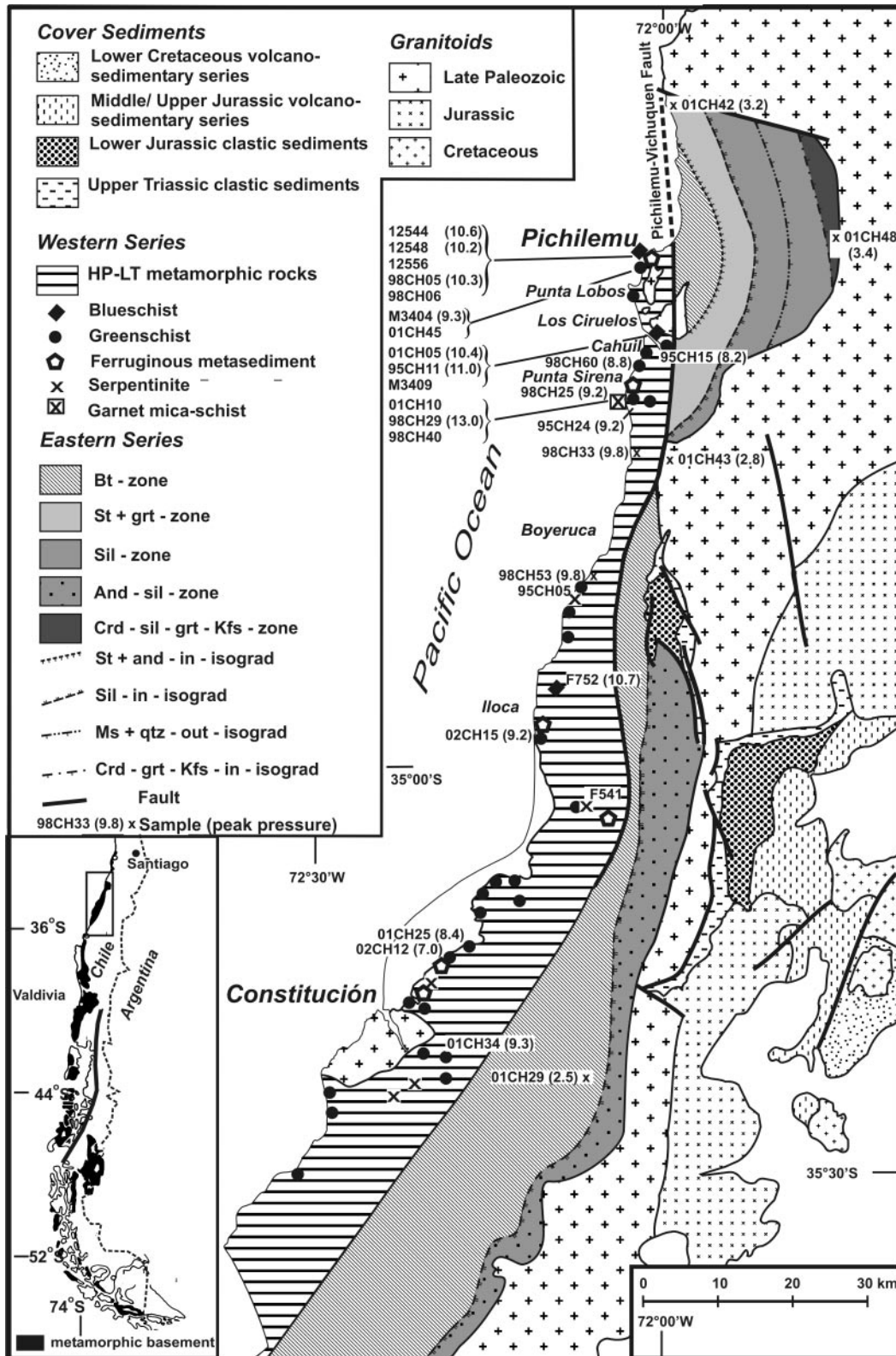
*E-mail: arne.willner@ruhr-uni-bochum.de

Fig. 1. Geological map of the paired metamorphic belt within the basement of the Coastal Cordillera in north–central Chile (34° and 35°30′S) and its cover rocks. Information is included from Godoy (1970), González Bonorino (1971), Moraga (1981), Gana & Hervé (1983), Bravo Espinosa (2001) and the author's own observations.

be deduced from the different lithologies present? What governs the metamorphic reaction history in the accretionary prism? Did peak pressures vary regionally and between rock types? Why is blueschist a very rare rock type in the high-pressure belt? How is metamorphism related to penetrative deformation? What is the nature of the metamorphic overprint during exhumation? What is the character of metamorphism in the concomitant high-temperature belt? Is it possible to reconstruct the fossil thermal structure of the paired metamorphic belt from the restricted information preserved within its rocks?

GEOLOGICAL SETTING AND FIELD RELATIONSHIPS

Traditionally the basement of the Coastal Cordillera has been subdivided into two metamorphic complexes (the Western and Eastern Series; Fig. 1), representing contrasting forearc environments. This association is a fundamental feature of the basement that can be observed consistently throughout the Coastal Cordillera despite variable ages of deposition, metamorphism and deformation. The concept was introduced by Aguirre *et al.* (1972) and summarized by Hervé (1988). The Western Series comprises low-grade metapsammopelitic rocks with a dominant transposition foliation and metabasite intercalations, whereas the Eastern Series lacks metabasites and is represented by a less deformed, very low grade metagreywacke–pelite sequence. Whereas the Western Series is regarded as an accretionary prism, the Eastern Series is considered to represent the retro-wedge area (Hervé, 1988; Willner *et al.*, 2000). In central Chile the Eastern Series is partly intruded by calc-alkaline plutons of a late Palaeozoic arc with an associated low-pressure–high-temperature metamorphic overprint.

In the Western Series (Fig. 1) the predominant rocks are former turbiditic deposits characterized by a penetrative, mainly subhorizontal transposition foliation with pronounced banding. This represents a second, or locally a third, foliation with frequent intrafolial folding of relic bands, which mostly lacks kinematic indicators and represents ductile thinning. Quartz veins of decimetre thickness transposed parallel to the penetrative foliation are prominent, but deformed cross-cutting quartz veins and undeformed subvertical, quartz-filled tension gashes also exist. Younger subparallel shear bands with variable transport directions are rare. Stretching lineations are characteristically subparallel to the mesoscopic fold axes and mainly NW–SE-trending in the southern part of the area, but varying in the north. Frequently black, postkinematic, albite porphyroblasts are present, locally giving rise to spotted schists. Whereas the metapsammopelitic schists lack garnet, an exceptional garnet mica-schist occurs only in the area of Punta Sirena (Fig. 1). This rock is characterized by abundant porphyroblasts of garnet of 2–10 mm size, by a brighter colour caused by predominant white mica and by a coarser grain size. It forms several layers of 10 m thickness at two localities north and south of Punta Sirena.

Metabasite intercalations in the Western Series make up only 15–20% of the rock volume, forming lenses of metre to kilometre size. Whereas these are commonly greenschist, blueschist was observed as rare lenses of 1–5 m thickness at three localities (Fig. 1: Infiernillo beach, Pichilemu; El Molino gorge, eastern Cahuil; a gorge NE of Iloca). Occasional green rims around these lenses are due to intensive retrograde growth of chlorite. In the greenschist lenses relic depositional features can be observed locally. At Infiernillo beach and at Punta Lobos (Fig. 1) pillow structures of 20–50 cm diameter are preserved with radial fractures filled with calcite and amygdules towards the centre of the pillows. At Infiernillo beach relic pyroclastic structures also occur: lenticular clasts (1–10 cm) of massive dark greenschist with abundant amygdules float in a more foliated matrix richer in ferromagnesian minerals. The structure strongly resembles former hyaloclastite. Also, the presence of relatively abundant white mica-bearing metabasite may point to the presence of former tuffitic deposits. According to Godoy (1986), the chemical composition of the metabasites (particularly immobile trace elements) throughout the basement of the Coastal Cordillera resembles that of mid-ocean ridge basalts (MORB) or intraplate basalts. Zones of enhanced fluid flow are indicated by: (1) layers or irregular zones of centimetre to metre scale characterized by phase reduction (e.g. monomineralic zones of epidote or chlorite); (2) concentrations of white albite porphyroblasts; (3) veins filled with quartz, albite, locally calcite and amphibole. The structural inventory of the metabasites is similar to that of the metapsammopelitic schists. Mesoscopic folds of centimetre to metre scale are more prominent and amphibole is often oriented parallel to the regional stretching lineation.

Several minor rock types are associated with the metabasites: (1) rare serpentinite lenses of several tens of metres in extent; (2) local layers of marble, black graphite-rich metapelite and pure quartzite of centimetre to metre thickness (metachert; Hervé, 1988); (3) prominent intercalations of ferruginous metasediments of centimetre to metre thickness. These last rocks comprise mainly stilpnomelane-bearing schists and quartzites partly with garnet and/or concentrations of magnetite of economic value (e.g. at Punta Sirena; Fig. 1) as well as layers of massive sulphide of centimetres thickness. In south–central Chile such rocks also grade into Mn-rich sediments (spessartine quartzites; 'coticules') which are regarded as pre-metamorphic Mn- and Fe-rich

hydrothermal precipitates mixed with aluminous alteration-derived material at the surface of the oceanic crust (Willner *et al.*, 2001). A similar origin is also possible for the ferruginous metasediments. The metabasites and their associated rock types appear to represent the upper part of segments of oceanic crust incorporated into the accretionary prism.

In the Eastern Series metabasic intercalations are absent and metagreywacke–pelite alternations prevail with occasional calcsilicate. Particularly in the central part of the exposed Eastern Series in the study area stratigraphic coherence of strata and well-preserved turbiditic sedimentary structures (cross-bedding, load casts, convolute bedding, graded bedding) are observed as well as slightly east-vergent folding of bedding by chevron folds up to 10 m wide. These rocks are overprinted by a flat west-dipping second foliation, which becomes a transposition foliation approaching the Western Series. Early formed quartz veins are frequent, but albite porphyroblasts are absent. In the study area, the Eastern Series is overprinted by a HT metamorphic event. The earlier stages of its tectono-thermal evolution under very low grade conditions can only be inferred by comparison with other areas in Chile, where the HT overprint is lacking (Hervé, 1988; Willner *et al.*, 2000). González Bonorino (1971) mapped several prograde north–south-trending metamorphic zones with the metamorphic grade increasing towards the axis of the batholith, which intrudes the Eastern Series at its eastern flank. Incipient biotite growth coincides with the western boundary of the Eastern Series. In the north of the study area garnet and oligoclase appear shortly before the staurolite isograd, which delimits the following zone characterized by garnet, staurolite and andalusite porphyroblasts. Then sillimanite appears and the highest grade zone is characterized by a migmatitic garnet–cordierite–sillimanite–K-feldspar gneiss. In the southern part of the study area staurolite does not appear and temperatures did not overstep the andalusite–sillimanite transition. The porphyroblasts grew postkinematically after the first and second deformation. However, local slight rotation of the porphyroblasts is observed, as well as occasional stretching of andalusite blasts and quartz-filled tension gashes parallel to the regional stretching lineation. This indicates that deformation continued with lesser intensity after the peak of the HT event within a stress field similar to that before this overprint.

At three localities (Pichilemu, eastern Punta Lobos, southern Boyeruca; Fig. 1) a north–south-striking semibrittle mélange-type shear zone occurs related to late-stage destruction of the accretionary prism. The boundary between the Eastern and Western Series in the north of the study area is a brittle reverse fault (Pichilemu–Vichuquén Fault; Fig. 1), which cuts the isograds in the Eastern Series, whereas in the south of the study area the boundary is transitional, as observed by Godoy (1970). The prominent fault is a further late deformation, which caused shortening of the accretionary prism.

Tonalite, granodiorite and granite dominate in the eastern part of the study area, forming part of the Southern Coastal Batholith (SCB) of Permo-Carboniferous age (Hervé *et al.*, 1988). Granite with magmatic muscovite is frequently observed, but granitoids also occur containing hornblende and titanite. S-type granitoids seem to be abundant in the SCB consistent with their high $^{87}Sr/^{86}Sr$ ratios (Hervé *et al.*, 1988). Lucassen *et al.* (2004) showed that isotope ratios of Nd and Pb are similar to those of the Palaeozoic metasediments, indicating a magmatic arc with a high crustal component. The Western Series are intruded by three small isolated bodies of biotite granite (Fig. 1; from north to south the plutons of Pichilemu, Los Ciruelos and Constitución). Scattered, local, post-tectonic basalt dykes of decimetre to metre thickness and a few rhyolitic dykes occur throughout the area. The Eastern Series and the batholith are unconformably overlain by Late Triassic to Early Cretaceous marine siliciclastic sediments and volcanic rocks.

PETROGRAPHIC CHARACTERISTICS OF THE WESTERN SERIES
Rock fabric
Metabasites

The mineral assemblage of the greenschists is amphibole–chlorite–epidote–albite–quartz $\pm$ titanite $\pm$ magnetite $\pm$ white mica $\pm$ calcite. Amphibole, chlorite and white mica (0·05–0·2 mm) are oriented parallel to the penetrative foliation, but cross-cutting grains are frequent. The recrystallized amphibole is always euhedral, forms up to 2 mm long needles and is strongly zoned, displaying bluish cores grading into green rims. Faint internal crenulation with recrystallized hinge zones can be detected within the dominant foliation. Epidote occurs as euhedral, optically zoned crystals of 0·1 mm size cross-cutting the fabric. Epidote and chlorite can continuously replace the existing assemblage until monomineralic layers are formed. Titanite forms small pods or trails of tiny anhedral grains (0·01–0·04 mm) parallel to the foliation with some relic crenulation hinges or larger euhedral recrystallized grains (0·1 mm). Quartz, albite and/or calcite form small polygonal aggregates or cross-cutting veinlets including all minerals of the matrix assemblage. Occasional anhedral albite porphyroblasts (0·1–0·5 mm) with internal trails of epidote and amphibole have grown after formation of the predominant foliation and across relic crenulation hinges. They may be rotated in rare

sheared rocks. Opaque phases are pyrite or magnetite which grew as large, euhedral, recrystallized grains (0·5–1 mm). Clinopyroxene (0·1–0·5 mm) is a ubiquitous relic of the protolith assemblage. It often has irregular grain boundaries as a result of replacement by surrounding minerals. In some cases, large clinopyroxene crystals still display their original euhedral outline as former phenocrysts. In rare sheared rocks the mineral shows brittle deformation and rotation. Further relic fabric are occasional amygdales (1–5 mm size) filled with albite and/or calcite. The amygdales are slightly flattened in the more strongly deformed areas.

The mineral assemblage of the rare blueschists is blue amphibole–chlorite–epidote–albite–quartz ± white mica ± titanite ± magnetite ± calcite. Banding at millimetre to centimetre scale is represented by dark bands of weakly oriented euhedral amphibole, chlorite, epidote and white mica (0·05–0·2 mm), alternating with bright bimineralic bands (amphibole–quartz, amphibole–epidote, amphibole–chlorite) or monomineralic strings (amphibole, chlorite, titanite, white mica or epidote). Crenulation of a relic foliation can also be observed within the bands, with oriented minerals recrystallizing in the crenulation hinges. Epidote and amphibole are optically zoned. Green amphibole overgrows blue amphibole along the rims. One sample (12544) contains relic clinopyroxene (0·5 mm). Unoriented euhedral albite crystals of similar size occur near the clinopyroxene crystals, suggesting a further magmatic relic. Quartz–albite veinlets with some blue amphibole occur parallel to the bands or cut across.

At four localities serpentinite lenses of 10 m scale are associated with the greenschist. Clinopyroxene occurs as the only relic phase forming a network of mainly 0·5 mm crystals, which surround other, entirely replaced phases with partly euhedral outline. Replacement minerals are mainly antigorite, minor tremolite and chlorite with exsolved magnetite. The original fabric resembles that of an ultramafic igneous cumulate. Godoy & Kato (1990) also decribed pyroxene relics and abundant layered magnetite concentrations in serpentinite from south–central Chile pointing to a similar origin.

Ferruginous metasediments

The three recognized types of iron-rich metasediments—stilpnomelane quartzite, stilpnomelane schist and magnetite–stilpnomelane rocks—can grade into each other and into the associated greenschist. The typical mineral assemblage is magnetite–stilpnomelane–amphibole–garnet–quartz–albite ± white mica ± chlorite ± epidote.

Stilpnomelane (0·1–0·3 mm) is unoriented in a polygonal quartz fabric in the stilpnomelane quartzites, with occasional chlorite, white mica, amphibole and rare trails of tiny, optically zoned garnet (0·01–0·05 mm), or forms nearly monomineralic layers of oriented and cross-cutting crystals (0·05–0·5 mm) in the stilpnomelane schists. Occasional unoriented porphyroblasts of albite or magnetite (0·4–0·8 mm) grow across the stilpnomelane. The rocks are mostly banded at a millimetre scale, containing some rootless, isoclinal, intrafolial microfolds with recrystallized fold hinges. Monomineralic pods of magnetite, stilpnomelane, garnet (0·01–0·05 mm) or epidote occur with a polygonal fabric.

Metapsammopelitic schist

The typical mineral assemblage of the monotonous metapsammopeltic schist is quartz–albite–white mica–chlorite–ilmenite ± magnetite ± epidote. The heavy mineral assemblage is characterized by zircon, apatite and tourmaline. There is prominent banding of alternating quartz- and phyllosilicate-rich bands of millimetre thickness. Quartz and albite (0·05–0·30 mm) form a polygonal fabric without relics of former detrital or oriented grains, but with local subgrain formation and sutured grain boundaries indicating late continuous deformation. White mica and chlorite (0·1–0·3 mm) are intensively intergrown showing a relic orientation. Crenulation hinges of various generations (F_2, F_3) are prominent, but the phyllosilicates are recrystallized in the hinges with frequent growth of cross-cutting mica. Albite porphyroblasts (0·5–2 mm) are a late, mostly unoriented phase and an intrinsic feature of the metapsammopelitic schist, overgrowing fold hinges of all generations (F_2, F_3). They are often macroscopically black as a result of internal inclusion trails of graphite, which trace relic crenulation hinges. The porphyroblasts are bound to the phyllosilicate-rich bands, growing at the expense of white mica. In some cases they can completely replace the white mica, forming bands of albite. The porphyroblasts are euhedral or partly anhedral as a result of incomplete development of the crystals or late pressure solution at the rims. Apart from this feature, local slight rotation of the porphyroblasts also indicates continuing weak deformation after the growth of the porphyroblasts.

The assemblage of the unusual garnet mica-schist at Punta Sirena is garnet–quartz–albite–white mica–chlorite–epidote–titanite ± ilmenite ± rutile. Garnet porphyroblasts range from 1 to 10 mm size with internal sigmoidal trails of titanite, ilmenite or quartz (0·01–0·05 mm). Near the rims the garnet overgrows a polygonal fabric of coarser quartz (0·05–0·3 mm), similar to that of the surrounding matrix. The grains are euhedral or partly replaced at the rims by white mica and chlorite; in some samples they are also replaced along cracks by chlorite and epidote. Dominant white mica and minor chlorite (0·2–0·5 mm) form two foliations within a matrix of polygonal quartz and albite. The phyllosilicates

recrystallize in crenulation hinges and cross-cutting grains are abundant. An early white mica occurs as inclusions in garnet and titanite. Subhedral grains of unoriented epidote (0·05–0·10 mm) are abundant in the foliation planes. Titanite forms euhedral, unoriented crystals of 0·1–0·5 mm size in the matrix, occasionally enclosing round rutile. Albite forms prominent, unoriented porphyroblasts (0·2–0·5 mm) enclosing trails of graphite, epidote, white mica, titanite or garnet. Some garnet mica-schist samples show a prominent orientation of the phyllosilicates parallel to the prevailing foliation. In these porphyroblasts of garnet, albite and titanite are strongly rotated, indicating a late, localized, non-coaxial deformation.

Mineral chemistry

Mineral compositions were determined using a Cameca SX 50 electron microprobe at Ruhr-Universität Bochum, Germany. Operating conditions were an acceleration voltage of 15 kV, a beam current of 15 nA, 20 s counting time per element on the peak and on the background and a defocused beam of 8 μm diameter to avoid loss of alkalis in micas, feldspars and amphiboles. Standards used were synthetic pyrope (Si, Al, Mg), rutile (Ti), glass of andradite composition (Ca, Fe), jadeite (Na), K-bearing glass (K), topaz (F), Ba-silicate glass (Ba, La). The PAP procedure was used for matrix correction. Representative analyses and structural formulae of minerals used for PT calculations, together with the calculation procedure of the structural formulae, are presented in Table 1. Further data are available as supplementary data tables which may be downloaded from http://www.petrology. oupjournals.org or upon request to the author. Element distribution maps were simultaneously produced for three elements by stepwise scanning over rectangular areas. Abbreviations for minerals and mineral components used throughout the text follow Kretz (1983), if not indicated otherwise. Whole-rock analyses were performed at Ruhr-Universität Bochum by XRF except Fe^{2+} and H_2O (standard wet chemical methods).

Clinopyroxene

The clinopyroxene is augite of probable magmatic origin and, hence, the only abundant relic of the protolith of some metabasites. Its composition (Table 1) varies widely: diopside$_{35-68}$, hedenbergite$_{1-15}$, enstatite$_{0-13}$, acmite$_{0-28}$, Tschermak component$_{0-28}$ with notable traces of Ti [0·01–0·06 atoms per formula unit (a.p.f.u.)] and Cr (0·00–0·03 a.p.f.u.). The clinopyroxene compositions follow a similar trend within all the samples analysed, which overlaps the compositional range of clinopyroxene in within-plate alkali basalts in a $MnO–TiO_2–Na_2O$ variation diagram (Nisbet & Pearce 1977; Fig. 2). This comparison is corroborated by the relatively low SiO_2 (44·7–45·9 wt %) and relatively high Na_2O (0·2–2·8 wt %), Al_2O_3 (2·1–6·9 wt %) and TiO_2 (0·5–2·2 wt %) contents of the clinopyroxenes. Most Ca + Na contents exceed 0·9 a.p.f.u., which is characteristic for alkaline igneous rocks (Leterrier et al., 1982). The relic clinopyroxene from serpentinite sample F541 also plots on the same trend, suggesting that it may represent former cumulus pyroxene within ultramafic cumulates in the oceanic crust. The above data suggest, therefore, that part of the accreted oceanic crust may have included ocean island basalts.

Garnet

Garnet in the Western Series is restricted to the unusual garnet mica-schist and the ferruginous metasediments. The garnet mica-schist contains a grossular-rich garnet with the compositional range almandine$_{0·47–0·76}$, grossular$_{0·14–0·34}$, spessartine$_{0·01–0·21}$, pyrope$_{0·02–0·09}$ (X_{Mg} 0·02–0·13, Ti ≤ 0·04; Table 1). Zoning is typically prograde and bell-shaped with an increase in Ca and Mg and a decrease in Mn, Fe^{2+}, Fe^{3+} and Ti from core to rim. Zonation of Ca is distinctly oscillatory.

In the ferruginous metasediments, the garnet is Mn- and Ca-rich with the compositional range almandine$_{0·14–0·47}$, spessartine$_{0·27–0·56}$, grossular$_{0·18–0·26}$, pyrope$_{0·01–0·03}$, uvarovite$_{0·06–0·07}$, andradite$_{0·01–0·04}$ (X_{Mg} 0·06–0·12, Ti ≤ 0·04 a.p.f.u.). These compositions are rather similar to that of garnet in the spessartine quartzite (coticule) in other parts of the basement, which have a pre-metamorphic hydrothermal origin (Willner et al., 2001). Zonation is prograde and bell-shaped with an increase in Ca, X_{Mg}, Mg and Fe^{2+} and a decrease in Mn and Fe^{3+} from core to rim.

Amphibole

At the three blueschist localities (see above; Fig. 1) Na-amphibole varies from glaucophane to magnesioriebeckite in composition (Fig. 3a; Table 1; nomenclature after Leake et al., 1997) and covers a wide, continuous range of $X_{Fe^{3+}}$ (0·21–1·00) and Na^B (= Na^{M4} = 1·51–1·93 a.p.f.u.) with more restricted X_{Mg} (0·52–0·85). Towards the rims the Na-amphibole continuously grades into NaCa-amphibole and actinolite (Fig. 3b; Fig. 4). The NaCa-amphibole is winchite (Na^B 0·50–1·49 a.p.f.u., Na^A < 0·28 a.p.f.u., X_{Mg} 0·63–0·93, $X_{Fe^{3+}}$ 0·29–1·00, Si 7·43–8·00 a.p.f.u.), which is partly ferrian (Fe^{3+} 0·75–1·74 a.p.f.u.) pointing to a relatively oxidized environment. At the outer rims actinolite occurs (Na^B 0·21–0·49 a.p.f.u., Na^A < 0·21 a.p.f.u., X_{Mg} 0·68–0·79, $X_{Fe^{3+}}$ 0·63–0·98, Si 7·45–7·88 a.p.f.u.; Fig. 4).

In the greenschist and the ferruginous metasediments, amphibole mostly grades from NaCa-amphibole to Ca-amphibole or is Ca-amphibole with a high Na^B content (Fig. 3c; Table 1). This variation also corresponds to high Na^B in the core decreasing towards the rims. The

Table 1: Representative mineral analyses (the complete dataset, including all compositions used for calculations, is available as an Electronic Appendix from http://www.petrology.oupjournals.org)

| | Clinopyroxene | | | Garnet | | | | | | | | |
| | Ultrabasite | Greenschist | Blueschist | Fe-meta-sediment | | Garnet mica-schist | | Eastern Series mica-schist | | Gneiss | |
	F541	01CH45	12544	98CH25C	98CH25R	01CH10C	01CH10R	98CH43C	98CH43R	01CH48C	01CH48R
SiO_2	49·09	50·47	50·03	35·85	35·97	36·52	37·09	36·22	35·96	36·36	36·31
TiO_2	1·90	0·87	0·84	0·01	0·00	0·28	0·16	0·07	0·01	0·00	0·08
Al_2O_3	4·89	2·75	3·58	19·02	20·14	20·91	21·47	21·01	21·07	21·26	21·18
Cr_2O_3	0·78	0·08	n.d.	0·01	0·00	0·03	0·02	n.d.	n.d.	n.d.	n.d.
Fe_2O_3*	1·14	3·33	2·62	2·58	1·52	0·69	0·08	0·12	0·38	0·85	1·12
FeO	4·07	4·87	4·92	12·17	14·91	21·58	26·44	31·98	39·08	35·90	36·06
MnO	0·17	0·18	0·14	23·56	18·76	10·24	2·53	8·43	1·26	1·40	1·35
MgO	14·62	14·76	15·08	0·40	0·76	0·46	1·55	1·12	1·42	3·69	3·46
CaO	22·57	22·27	21·74	6·99	7·87	9·28	10·43	1·25	1·05	0·93	1·27
Na_2O	0·26	0·27	0·17								
Sum	99·49	99·85	99·12	100·59	99·93	99·99	99·77	100·20	100·23	100·39	100·83
Si	1·822	1·878	1·867	5·953	5·912	5·898	5·926	5·925	5·888	5·856	5·834
Al^{IV}	0·178	0·122	0·133	0·047	0·089	0·102	0·074	0·075	0·112	0·144	0·166
Al^{VI}	0·036	0·000	0·025	3·675	3·812	3·879	3·969	3·976	3·952	3·891	3·846
Ti	0·053	0·024	0·024	0·001	0·000	0·034	0·020	0·009	0·001	0·000	0·010
Cr	0·023	0·002	n.d.	0·002	0·000	0·004	0·002	n.d.	n.d.	n.d.	n.d.
Fe^{3+}	0·032	0·093	0·073	0·323	0·188	0·083	0·009	0·015	0·047	0·109	0·144
Fe^{2+}	0·126	0·152	0·154	1·367	1·861	2·915	3·533	4·375	5·350	4·835	4·846
Mn	0·005	0·006	0·005	0·099	0·186	0·111	0·368	0·272	0·346	0·885	0·829
Mg	0·809	0·818	0·839	3·314	2·612	1·401	0·342	1·167	0·175	0·192	0·184
Ca	0·898	0·886	0·869	1·244	1·386	1·606	1·785	0·219	0·184	0·160	0·219
Na	0·019	0·020	0·012								

*Normalization to four cations to calculate Fe^{3+}.
For garnet, cations based on 48 valencies including 10 cations in the tetrahedral and octahedral sites to calculate Fe^{3+}. C, core; R, rim; n.d., not determined.

Table 1: continued

White mica

	Blueschist		Greenschist		Fe-meta-sediment	Metapsammopelitic schist		Garnet mica-schist		Eastern Series mica-schist		Granite
	98CH05	98CH05	01CH34	01CH34	98CH25	98CH33	98CH33	01CH10	01CH10	01CH29	01CH43	98CH43
	I	II	I	II	I	I	II	I	II	Bt-zone	Stau-zone	
SiO_2	51·20	49·86	47·66	46·21	47·16	48·97	47·07	49·89	48·16	44·36	45·37	45·09
TiO_2	0·06	0·06	0·23	0·26	0·04	0·19	3·44	0·08	0·33	0·16	0·25	0·16
Al_2O_3	22·40	22·87	28·61	29·32	25·11	30·14	29·33	28·06	30·26	36·17	37·50	35·56
Cr_2O_3	0·20	0·35	0·05	0·14	0·02	0·03	0·00	0·03	0·07	0·00	0·05	0·00
FeO	4·59	5·24	3·18	3·21	6·73	1·97	1·94	2·69	2·31	1·27	1·25	1·36
MnO	0·01	0·05	0·01	0·03	0·09	0·02	0·02	0·01	0·02	0·01	0·03	0·12
MgO	4·57	5·12	2·97	2·90	2·94	2·55	2·18	3·02	2·50	0·45	0·26	0·57
CaO	0·21	0·00	0·00	0·00	0·02	0·00	0·01	0·00	0·00	0·00	0·00	0·00
BaO	0·35	0·32	0·35	0·60	1·70	0·26	0·20	0·61	0·41	0·31	0·30	0·17
Na_2O	0·31	0·11	0·22	0·23	0·25	0·29	0·33	0·40	0·92	1·18	1·77	0·48
K_2O	10·53	10·40	10·94	10·74	10·23	10·43	10·64	10·23	9·63	9·92	8·51	10·06
H_2O^*	4·38	4·42	4·39	4·37	4·31	4·42	4·44	4·45	4·46	4·42	4·53	4·37
Sum	98·91	99·33	98·61	98·01	98·99	99·36	99·600	99·47	99·07	98·26	99·82	97·94
Si	7·003	6·764	6·503	6·347	6·569	6·550	6·334	6·703	6·480	6·023	6·173	6·094
Al^{IV}	0·997	1·236	1·497	1·653	1·431	1·450	1·666	1·297	1·520	1·977	1·827	1·906
Al^{VI}	2·614	2·421	3·104	3·092	2·690	3·300	2·986	3·146	3·279	3·811	3·694	3·759
Cr	0·022	0·038	0·005	0·015	0·002	0·003	0·000	0·004	0·007	0·000	0·000	0·000
Ti	0·006	0·006	0·023	0·027	0·004	0·019	0·348	0·008	0·034	0·017	0·013	0·016
Fe^{2+}	0·426	0·046	0·241	0·109	0·348	0·220	0·218	0·302	0·260	0·145	0·185	0·154
Fe^{3+}	0·099	0·549	0·122	0·260	0·436	0·000	0·000	0·000	0·000	0·000	0·000	0·000
Mn	0·002	0·005	0·001	0·004	0·010	0·000	0·002	0·001	0·002	0·002	0·009	0·014
Mg	0·931	1·036	0·604	0·594	0·610	0·509	0·437	0·604	0·502	0·092	0·153	0·115
Sum	4·100	4·100	4·100	4·100	4·100	4·054	3·992	4·065	4·084	4·066	4·054	4·058
Ca	0·031	0·000	0·000	0·000	0·003	0·000	0·001	0·000	0·000	0·000	0·000	0·000
Ba	0·019	0·017	0·019	0·032	0·093	0·014	0·010	0·032	0·022	0·016	0·007	0·009
Na	0·081	0·029	0·057	0·062	0·067	0·075	0·086	0·105	0·240	0·311	0·099	0·126
K	1·837	1·799	1·905	1·882	1·818	1·780	1·827	1·753	1·653	1·719	1·707	1·734
Sum	1·968	1·845	1·981	1·976	1·980	1·869	1·924	1·890	1·914	2·046	1·812	1·869
OH	4·000	4·000	4·000	4·000	4·000	4·000	4·000	4·000	4·000	4·000	4·000	4·000

The proportion of cations is based on 42 valencies neglecting the interlayer cations; the sum of octahedrally coordinated cations is set at 4·1 to allow for an estimation of Fe^{3+}; the amounts of Cl and F are near or below detection limit.
*Amount calculated.

Amphibole

	Blueschist		Greenschist		Ferruginous metasediment	
	98CH05 I	98CH05 II	01CH34 I	01CH34 II	98CH25 I	98CH25 II
SiO_2	56.30	53.64	50.57	54.29	50.33	54.14
TiO_2	0.04	0.02	0.19	0.03	0.03	0.03
Al_2O_3	6.09	2.53	7.17	3.22	7.36	1.95
Cr_2O_3	0.05	0.04	0.08	0.01	0.01	0.03
Fe_2O_3*	6.11	3.05	4.82	3.20	11.07	7.51
FeO	9.02	10.37	7.22	7.30	8.49	4.89
MnO	0.14	0.28	0.32	0.28	0.99	1.40
MgO	10.88	14.04	14.42	16.79	9.47	16.12
CaO	2.58	9.08	10.25	11.39	4.32	9.61
BaO	0.04	0.02	0.00	0.08	0.09	0.06
Na_2O	5.93	2.07	1.92	1.02	5.33	1.87
K_2O	0.03	0.40	0.17	0.06	0.15	0.09
H_2O*	2.12	2.01	2.06	2.09	2.06	2.11
Sum†	99.33	97.55	99.19	99.76	99.70	99.81
Si	7.954	7.853	7.252	7.680	7.318	7.698
Al^{IV}	0.046	0.147	0.748	0.320	0.682	0.302
Al^{VI}	0.968	0.290	0.464	0.218	0.579	0.024
Ti	0.004	0.003	0.020	0.003	0.003	0.003
Cr	0.005	0.004	0.009	0.001	0.001	0.003
Fe^{3+}	0.650	0.337	0.520	0.341	1.212	0.804
Fe^{2+}	1.066	1.269	0.866	0.863	1.032	0.582
Mn	0.017	0.034	0.038	0.034	0.122	0.169
Mg	2.290	3.064	3.082	3.540	2.052	3.415
Ca	0.390	1.424	1.575	1.727	0.672	1.464
Ba	0.002	0.001	0.000	0.005	0.005	0.004
Na	1.623	0.587	0.533	0.280	1.516	0.515
K	0.006	0.075	0.032	0.011	0.028	0.016
Sum	2.022	2.087	2.139	2.022	2.208	1.998
OH	2.000	2.000	2.000	2.000	2.000	2.000

Biotite

	Eastern Series Biotite zone	Stau–And zone	Kfs–Crd–Grt–Sil zone
	01CH29	01CH43	01CH48
SiO_2	33.15	33.74	33.91
TiO_2	1.65	1.80	3.44
Al_2O_3	18.33	19.47	19.04
FeO	24.92	25.19	21.20
MnO	0.14	0.07	0.05
MgO	6.77	5.80	7.89
CaO	0.00	0.02	0.00
BaO	0.00	0.14	0.31
Na_2O	0.04	0.31	0.35
K_2O	8.73	8.62	9.32
F	0.00	0.00	0.31
Cl	0.00	0.20	0.03
H_2O*	3.76	3.73	3.73
Sum†	97.49	99.09	99.47
Si	5.289	5.293	5.232
Al^{IV}	2.711	2.707	2.768
Al^{VI}	0.737	0.894	0.694
Ti	0.198	0.212	0.399
Fe^{2+}	3.325	3.306	2.735
Mn	0.019	0.009	0.007
Mg	1.610	1.355	1.814
Sum	5.888	5.776	5.649
Ba	0.000	0.009	0.019
Na	0.013	0.095	0.104
K	1.777	1.726	1.834
Sum	1.790	1.830	1.956
Cl	0.001	0.000	0.009
F	0.000	0.097	0.153
OH	3.999	3.903	3.838

For amphibole, the proportion of cations is based on 46 valencies and the sum of cations = 13 except for Ca. Na and K for estimation of Fe^{3+}. For biotite, cations based on 44 valencies.
*Value calculated.
†Sum corrected for F and Cl.

Table 1: continued

	Stilpnomelane Fe-meta-sediment	Staurolite mica-schist		Cordierite gneiss
	98CH25	95CH29	98CH49	01CH48
SiO_2	37·04	26·71	26·05	47·06
TiO_2	0·01	0·48	0·40	0·02
Al_2O_3	15·13	53·83	55·88	32·42
ZnO	0·01	0·29	0·01	
FeO	14·94	15·22	13·35	10·05
MnO	1·34	0·29	0·23	0·15
MgO	14·03	1·34	1·52	7·30
CaO	0·09			0·00
BaO	0·09			0·08
Na_2O	0·63			0·34
K_2O	4·48			0·01
H_2O*	5·36	1·05	1·05	
Sum	93·15	99·21	98·49	97·43
Si	6·213	3·816	3·708	4·948
Al^{IV}	2·787	0·184	0·292	1·052
Al^{VI}	0·204	8·881	9·083	2·964
Ti	0·001	0·052	0·001	0·002
Zn	0·001	0·030	0·043	0·000
Fe^{2+}	0·164	1·819	1·590	0·883
Fe^{3+}	1·932	0·000	0·000	0·000
Mn	0·190	0·035	0·027	0·014
Mg	3·507	0·286	0·322	1·145
Sum	6·000	11·104	11·066	5·007
Ca	0·016		0·001	
Ba	0·006		0·003	
Na	0·204		0·069	
K	0·959		0·001	
Sum	1·185		0·073	
OH	6·000			

For stilpnomelane, cations based on 47·375 valencies neglecting K + Na; Fe^{3+} is estimated assuming 15 cations. For staurolite, cations based on 47 valencies. For cordierite, cations based on 36 valencies.
*Value calculated.

Titanite

	Blueschist 98CH05	Greenschist M3404	Garnet mica-schist 98CH40
SiO_2	30·24	30·16	29·65
TiO_2	38·12	37·04	38·14
Al_2O_3	0·94	1·48	1·53
Fe_2O_3	1·46	1·44	0·20
MnO	0·01	0·00	0·01
CaO	28·83	28·36	29·15
F	0·21	0·33	0·21
H_2O^*	0·23	0·27	0·18
Sum†	100·50	99·08	99·07
Si	0·986	0·991	0·972
Ti	0·934	0·915	0·940
Al	0·036	0·057	0·059
Fe^{3+}	0·036	0·036	0·005
Ca	1·007	0·998	1·024
Mn	0·000	0·000	0·000
F	0·020	0·033	0·021
OH	0·050	0·058	0·040
O‡	4·921	4·907	4·913

Epidote

	Blueschist 01CH05 I	II	Greenschist 01CH34 I	II	Fe-meta-sediment 98CH25d	Garnet mica-schist 01CH10
SiO_2	37·66	36·90	37·72	37·66	36·27	37·85
TiO_2	0·02	0·12	0·18	0·10	0·03	0·37
Al_2O_3	23·13	21·43	27·74	24·90	21·39	26·92
Cr_2O_3	0·01	0·00	0·09	0·05	0·03	0·03
Fe_2O_3	13·29	14·61	7·80	11·38	14·76	8·68
Mn_2O_3	0·23	0·24	0·31	0·10	2·23	0·26
CaO	23·76	24·25	24·19	24·23	20·24	23·15
H_2O^*	3·76	3·66	3·77	3·76	3·63	3·78
Sum	101·86	101·21	101·80	102·18	98·58	101·04
Si	3·000	3·000	3·000	3·000	3·000	3·000
Al	2·172	2·054	2·601	2·338	2·0854	2·514
Cr	0·001	0·000	0·006	0·003	0·0017	0·002
Fe^{3+}	0·797	0·894	0·467	0·682	0·9186	0·517
Mn^{3+}	0·014	0·015	0·019	0·006	0·1401	0·016
Ti	0·001	0·007	0·011	0·006	0·002	0·022
Ca	2·028	2·113	2·062	2·068	1·7931	1·965
OH	2·000	2·000	2·000	2·000	2·000	2·000

For titanite, sum of cations is three; $OH = (Al + Fe^{3+}) - F$; Cl is below the detection limit. For epidote, the proportions of cations are based on a normalization of Si to three cations; F and Cl are at the detection limit.
*Value calculated.
†Sum corrected for amount of F.
‡$O = [(\Sigma \text{ positive valencies}) - OH - F]/2$.

Table 1: continued

	Chlorite								
	Blueschist 01CH05		Greenschist 01CH34		Fe-meta-sediment 98CH25	Garnet mica-schist 01CH10	Metapsammopelite 98CH33		Mica-schist 01CH29
	I	II	I	II			I	II	
SiO_2	27·23	27·05	26·39	26·73	27·39	25·70	26·27	25·91	25·56
TiO_2	0·06	0·00	0·05	0·04	0·01	0·00	0·05	0·03	0·10
Al_2O_3	18·92	19·30	21·14	20·92	19·42	14·84	21·30	21·61	19·32
FeO	23·15	21·80	18·03	17·87	18·16	25·86	22·97	23·51	32·29
MnO	0·27	0·33	0·17	0·13	1·55	0·48	0·37	0·41	0·24
MgO	16·85	17·96	21·25	21·24	19·79	20·45	15·66	15·98	10·27
H_2O^*	11·38	11·44	11·75	11·75	11·55	11·29	11·43	11·48	10·97
Sum	97·86	97·88	98·78	98·68	97·87	98·62	98·05	98·93	98·75
Si	5·740	5·670	5·386	5·455	5·662	5·457	2·755	2·707	2·795
Al^{IV}	2·260	2·331	2·614	2·545	2·338	2·544	1·389	1·368	1·205
Al^{VI}	2·440	2·437	2·469	2·486	2·412	2·574	2·015	2·055	1·285
Ti	0·009	0·000	0·008	0·006	0·002	0·000	0·004	0·003	0·009
Fe	4·082	3·822	3·077	3·049	3·151	4·591	2·015	2·055	2·952
Mn	0·048	0·059	0·030	0·022	0·272	0·086	0·033	0·037	0·023
Mg	5·295	5·611	6·464	6·460	6·120	4·697	2·448	2·489	1·673
OH	16·000	16·000	16·000	16·000	16·000	16·000	16·000	16·000	16·000

Cations based on 56 valencies; F and Cl are at the detection limit.
*Value calculated.
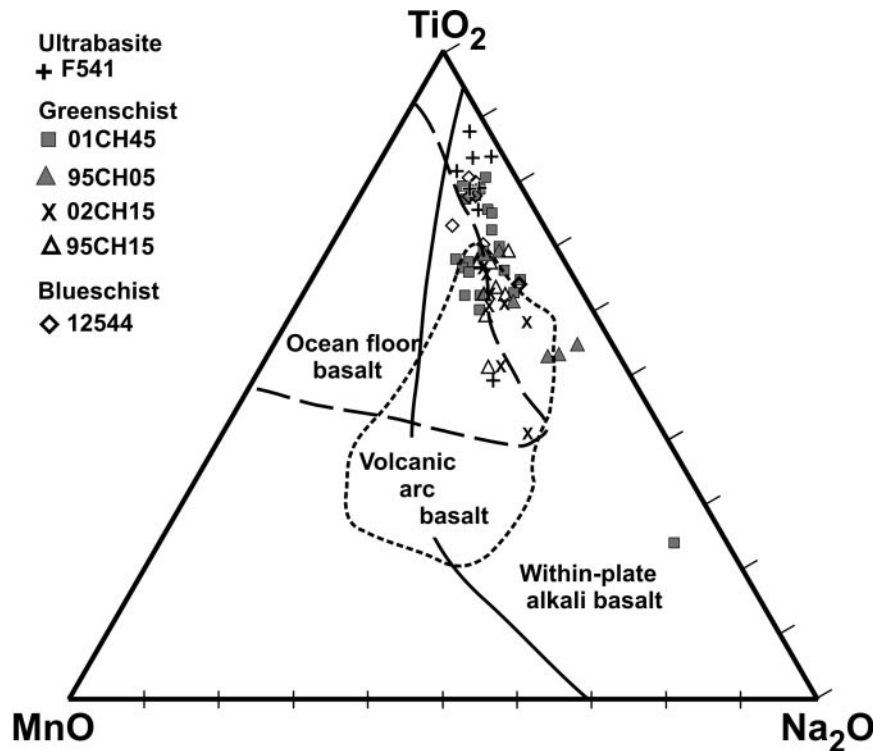
Fig. 2. MnO–TiO$_2$–Na$_2$O variation diagram (wt %) for magmatic clinopyroxene in metabasite and its compositional range in reference rock types (Nisbet & Pearce, 1977).

NaCa-amphibole (Na^B 0·50–0·88 a.p.f.u., Na^A 0·00–0·31, X_{Mg} 0·40–0·82, $X_{Fe^{3+}}$ 0·60–0·97) includes winchite (Si 7·50–7·93 a.p.f.u.) and barroisite (Si 6·64–7·48 a.p.f.u.). Barroisite is partly ferribarroisite (Fe^{3+} 1·23–2·00 a.p.f.u.) in the ferruginous metasediments. The Ca-amphibole (Na^B 0·02–0·49 a.p.f.u., Na^A 0·00–0·39, X_{Mg} 0·58–0·86, $X_{Fe^{3+}}$ 0·30–1·00) ranges gradually from actinolite (Si 7·58–7·93 a.p.f.u.) to magnesiohornblende (Si 7·00–7·48 a.p.f.u.). It is notable that, at a given Na^B content, the total R^{3+} content in the amphiboles of the greenschist is considerably higher than in those of the blueschist (Fig. 3b and c; except sample M3404). This may be due to a higher Tschermak substitution in the amphiboles of the greenschists leading in part to barroisite and magnesiohornblende compositions.

The overall compositional variation of amphibole during continuous grain growth, as well as between the peak metamorphic compositions of different blueschist and greenschist samples, shows complete transitions between Ca- and Na-amphibole, suggesting that no miscibility gap exists between Na- and Ca-amphiboles at the given conditions and compositions. Amphibole compositions can be plotted in terms of 'actinolite, glaucophane and riebeckite components' (Fig. 5a and b) showing complete solid-solution between Fe-rich Ca- and Na-amphiboles. The remaining possible solid-solution gap between

Mg-rich actinolite and glaucophane must be smaller than that calculated by Massonne (1995a, 1995b) at 300°C, indicating amphibole growth at $T > 300$°C.

White mica

White mica of phengite composition occurs in all rock types (Table 1). Si contents are highest in the blueschist (3·33–3·53 a.p.f.u.) with a variation of 0·10–0·15 a.p.f.u. in single samples, whereas the range is wider in the greenschist (3·14–3·5 a.p.f.u.) with mostly lower maximum contents and a similar range in individual samples (Fig. 6). Si contents are still lower in the metapsammopelites (3·10–3·30 a.p.f.u.), but also in the garnet mica-schist (3·2–3·36 a.p.f.u.). Ti and Na contents are very low in all rock types (<0·05 a.p.f.u.). Most compositions plot below the ideal Tschermak-substitution line in Fig. 6 owing to partial substitution of Al by Fe^{3+} and some di/trioctahedral substitution. Fe^{3+} contents were estimated by normalizing the sum of cations on the octahedral site to 2·05 a.p.f.u. (see Massonne, 1995a, 1995b). This is due to a restriction of the di/trioctahedral substitution experimentally detected by Massonne & Schreyer (1986) for white mica with variable Si contents. Calculated Fe^{3+} contents are highest in the magnetite-rich ferruginous metasediments (0·17–0·36 a.p.f.u.) and in the metabasites (<0·32 a.p.f.u.), which also contain Fe^{3+}-rich amphibole.
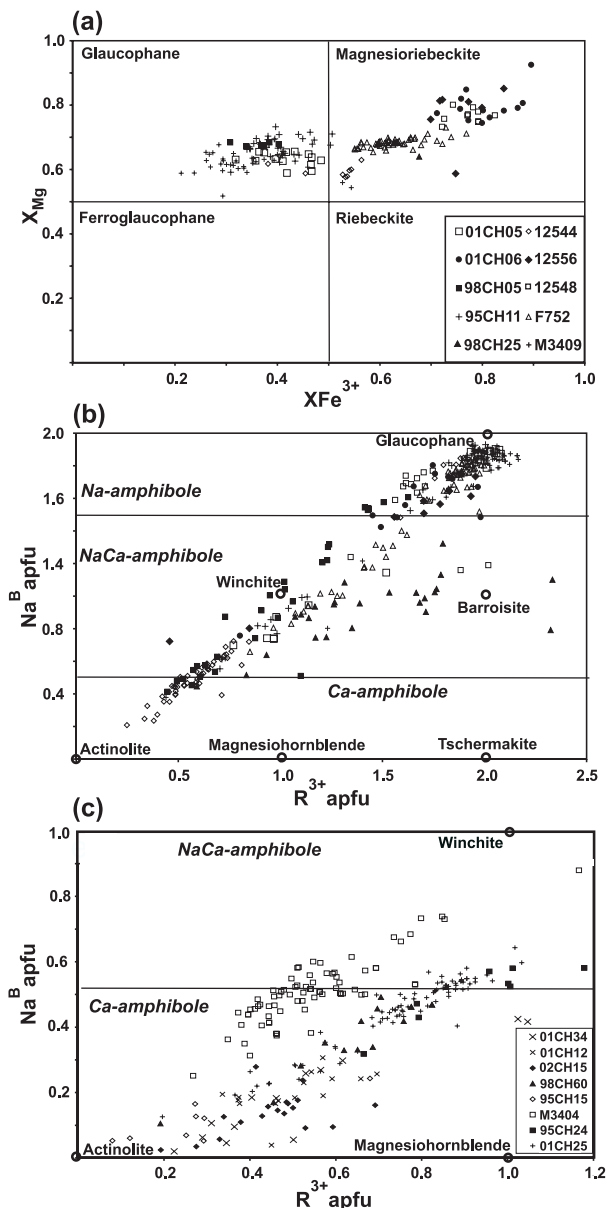
Fig. 3. Variation diagrams to illustrate amphibole compositions in blueschists (a, b; including ferruginous metasediment 98CH25) and greenschists (c).

No Fe^{3+} was estimated in the white mica of the metapsammopelites. In each metabasite sample there is a strong negative correlation of Si with Fe^{3+} that seems to be enriched in the Si-poor rims of phengite grains.

No unambiguous pattern of chemical zonation could be detected, but lower values of Si are mostly measured near the rims. Only in the ferruginous metasediments do notable Ba contents exist (0·03–0·07 a.p.f.u.), presumably representing a premetamorphic hydrothermal component. Relic prograde phengite is observed only in the garnet mica-schist, as inclusions in garnet and titanite;

this shows a slight chemical difference (Si 3·2–3·25 a.p.f.u., X_{Mg} 0·64–0·7, Na 0·07–0·12 a.p.f.u., Ti 0·15–0·3 a.p.f.u.) compared with the matrix white mica (Si 3·24–3·36, X_{Mg} 0·5–0·7, Na 0·02–0·07, Ti 0·005–0·01).

Chlorite, titanite, epidote, stilpnomelane

Chlorite compositions in the metabasites vary within a similar range (Si = 2·55–3·10 a.p.f.u.; X_{Mg} = 0·52–0·68). Among the minor elements only Mn has a notable abundance (0·02–0·17 a.p.f.u.). Chlorite in metapsammopelitic rocks has partly lower Si contents (2·52–2·74 a.p.f.u.) and X_{Mg} (0·31–0·55) than in the metabasites.

Titanite is a prominent accessory phase in the metabasites and in the garnet mica-schist with a $Ca(Al,Fe^{3+})SiO_4(F,OH)$-component between 4 and 52 mol %. Notable contents of F (0·02–0·59 wt %), Al (0·03–0·46 a.p.f.u.) and Fe^{3+} (0·01–0·22 a.p.f.u.) are observed. The Fe^{3+} content of epidote varies widely in different samples (0·44–0·99 a.p.f.u.), but generally an increase is observed from core to rim.

Stilpnomelane is the rock-forming mineral in the ferruginous metasediments, with notable contents of Mn (0·19–0·40 a.p.f.u.) and Na (0·11–0·23 a.p.f.u.).

PETROGRAPHIC CHARACTERISTICS OF THE EASTERN SERIES

Apart from very rare calcsilicate rocks, the Eastern Series are lithologically extremely homogeneous and mineral assemblages, fabric and mineral chemistry change in response to the zonation of the high-temperature metamorphic overprint.

Within the biotite zone the main assemblage is biotite–chlorite–muscovite–quartz–plagioclase ± ilmenite. The first biotite grew at the expense of white mica and chlorite, either as mimetic growth along oriented phyllosilicates or as porphyroblasts of 0·05–0·30 mm size. A polygonal fabric of quartz and plagioclase is prominent. In the biotite zone white mica is muscovite only (Si 3·00–3·16 a.p.f.u., Na 0·05–0·15 a.p.f.u., Ti 0·01 a.p.f.u.), plagioclase is oligoclase (15–19 mol % anorthite), whereas biotite (X_{Mg} 0·32–0·34, Ti 0·1 a.p.f.u.) and chlorite (Si 2·5–2·75 a.p.f.u., X_{Mg} 0·34–0·36, Mn 0·04–0·07 a.p.f.u.) are Fe-rich (Table 1). Compositional variation within and among samples is low.

A staurolite–andalusite zone is only observed in the north of the study area. Two main assemblages are: garnet–biotite–muscovite–plagioclase–quartz ± staurolite ± ilmenite and andalusite–biotite–muscovite–plagioclase–quartz ± staurolite ± ilmenite. Although porphyroblasts of garnet, biotite, staurolite and andalusite grew post-kinematically with respect to the penetrative
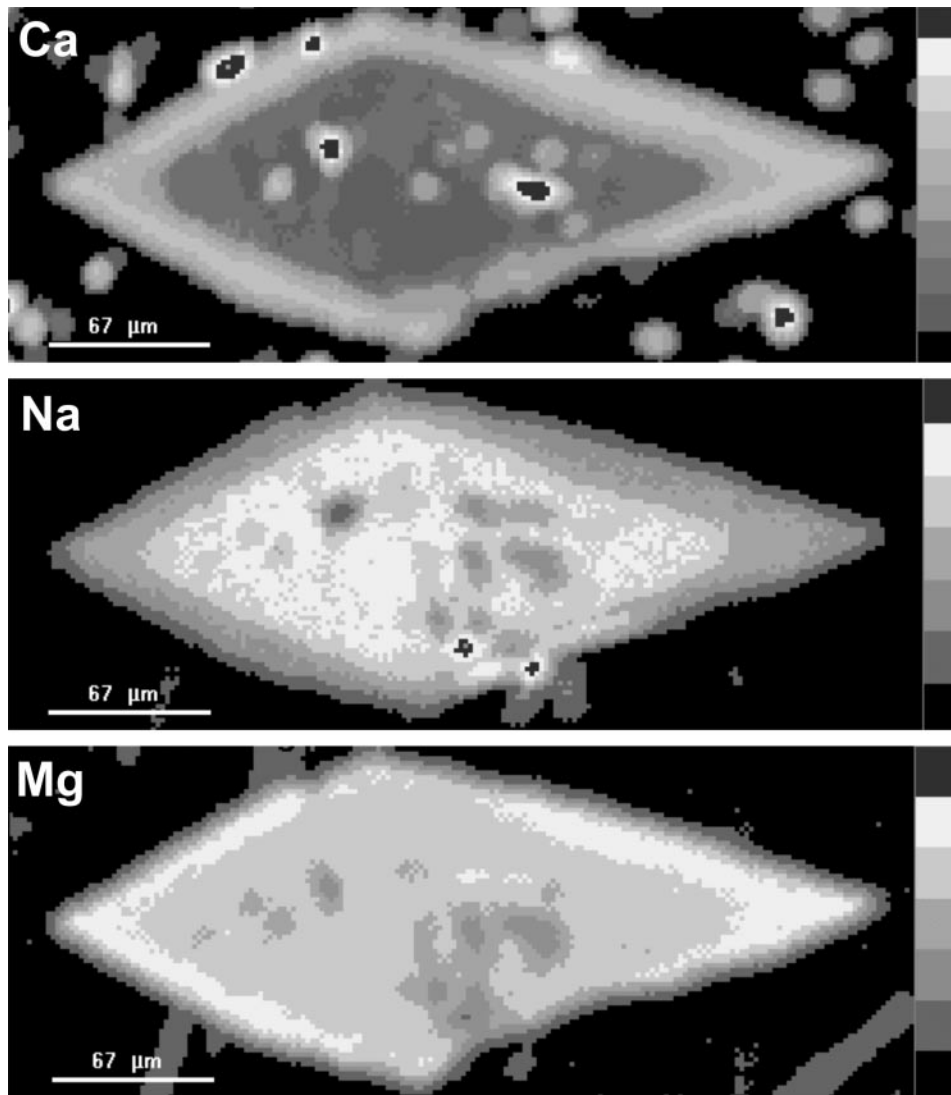
Fig. 4. Maps of X-ray intensity distribution for Ca, Na and Mg in a zoned glaucophane (core) overgrown by a Na–Ca-amphibole rim (blueschist sample 95CH11). Relative intensities increase from light to dark grey.

foliation, slight rotation is observed locally, indicating continuing deformation with waning intensity after the peak of HT metamorphism. Staurolite porphyroblasts (1–2 mm) are euhedral with tiny inclusions of quartz and biotite. At the rims slight replacement by muscovite, chlorite and ilmenite is observed. Small euhedral garnet porphyroblasts (0·1–0·3 mm) are nearly devoid of inclusions. The size of the prominent andalusite porphyroblasts ranges from 0·1 cm to several centimetres. Frequently, partial replacement by sericite and chlorite occurs, indicating very low temperature alteration. Also, quartz-rich calcsilicate rocks are locally observed containing the assemblage garnet–clinoproxene–quartz–plagioclase–titanite.

In the south of the study area medium-grade conditions are represented by an andalusite–sillimanite zone as the highest grade without appearance of staurolite. However, some poikilitic cordierite in the matrix has been described by Gana & Hervé (1983). Andalusite porphyroblasts are only of 1–2 mm size, but locally abundant. In the eastern part of the zone fibrolite appears replacing andalusite at the rims.

Medium-grade schists are characterized by muscovite (Table 1) with an increased paragonite component (Si 3·00–3·09 a.p.f.u., Na 0·20–0·27 a.p.f.u., Ti 0·01–0·017 a.p.f.u.), oligoclase (19–25 mol % anorthite), Mg-rich biotite (X_{Mg} 0·28–0·35, Ti 0·09–0·11 a.p.f.u.) and staurolite with traces of Mn and Zn (X_{Mg} 0·12–0·17, Mn 0·022–0·035 a.p.f.u., Zn 0·021–0·029 a.p.f.u.); garnet composition is almandine$_{0.73–0.89}$, pyrope$_{0.05–0.08}$, spessartine$_{0.03–0.19}$, grossular$_{0.02–0.02}$ (X_{Mg} 0·06–0·12, Ti ≤0·04 a.p.f.u.). Its zonation is bell-shaped with
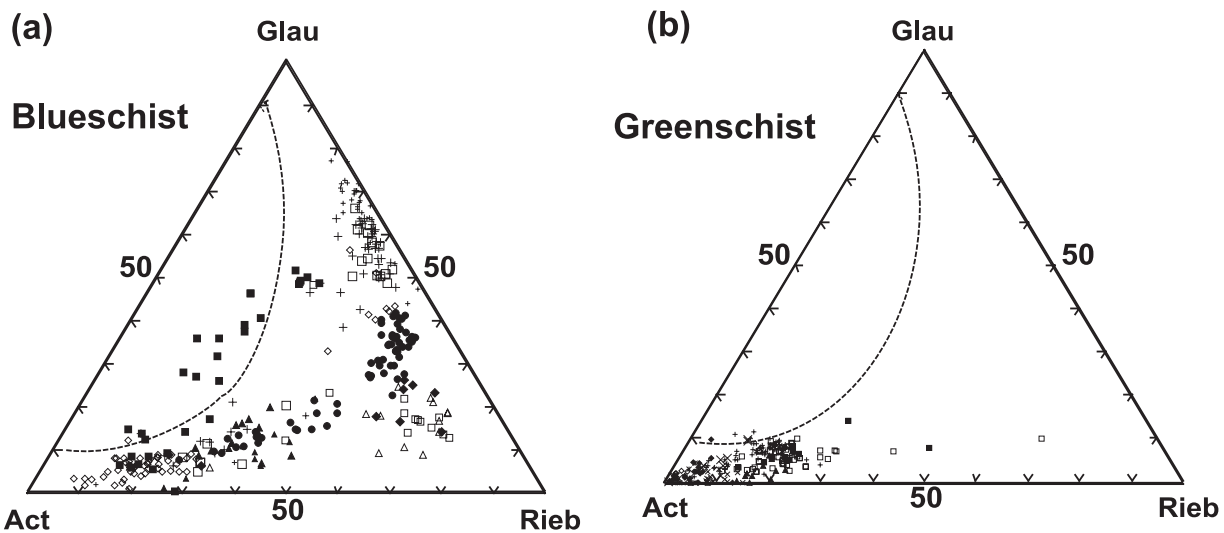
Fig. 5. End-member variation diagrams to illustrate amphibole compositions in blueschists [(a) including ferruginous metasediment 98CH25] and greenschists (b); $X_{Glau} = (2 - Ca)/2 \times {}^{VI}Al/({}^{VI}Al + Fe^{3+})$; $X_{Act} = Ca/2$; $X_{Rieb} = 1 - (X_{Rieb} + X_{Act})$ with calculated solvus (dashed line) from Massonne (1995a). Sample symbols as in Fig. 3.
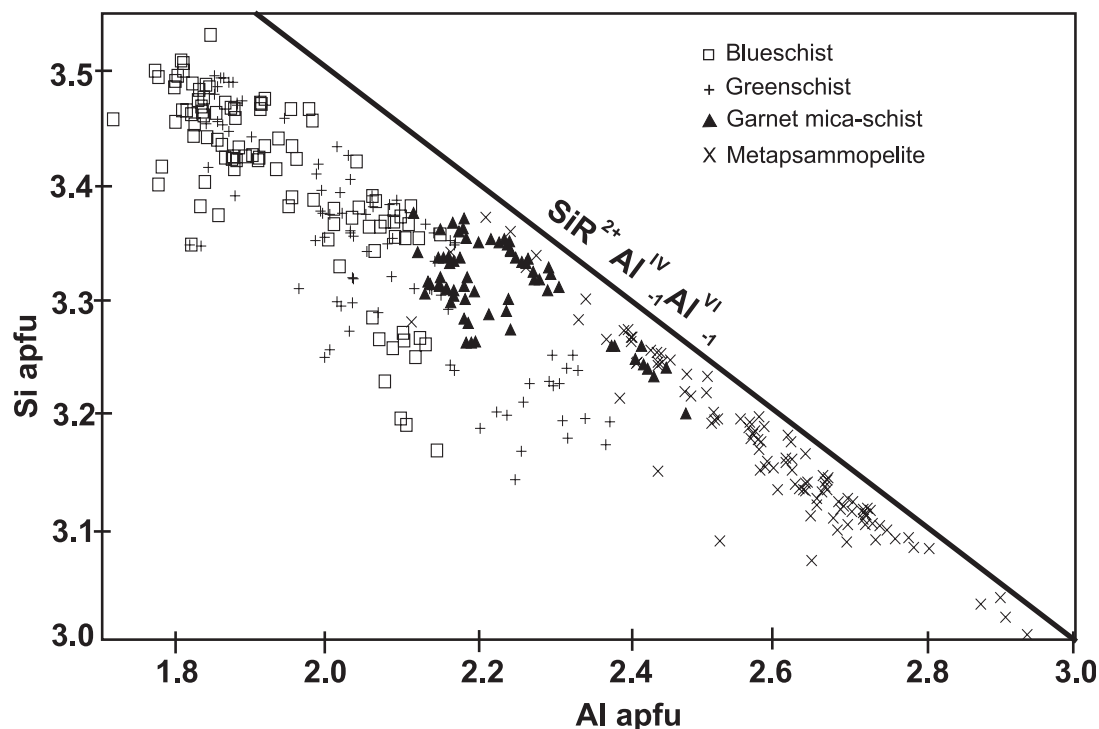
Fig. 6. Si–Al variation diagram of white mica within all the studied rock types. The line of the ideal Tschermak substitution is indicated.

decreasing Mn, Ca and Ti, and increasing Mg and Fe from core to rim. X_{Mg} remains constant.

In the highest grade zone of the northern study area a migmatitic gneiss with the assemblage garnet–cordierite–sillimanite–K-feldspar–plagioclase–quartz occurs. Garnet forms prominent anhedral porphyroblasts (0·5–1·0 cm) with inclusions of quartz, biotite and sillimanite

particularly near the rims. Garnet composition (Table 1) is almandine$_{0.79–0.81}$, pyrope$_{0.12–0.15}$, spessartine$_{0.02–0.03}$, grossular$_{0.02–0.04}$ (X_{Mg} 0·13–0·16, Ti $\leq$ 0·04 a.p.f.u.). The garnet is internally unzoned. Quartz and plagioclase (19–25 mol % anorthite) show secondary recrystallization of large crystals (0·3–0·8 mm) at the expense of smaller ones with abundant inclusions of biotite, fibrolite and
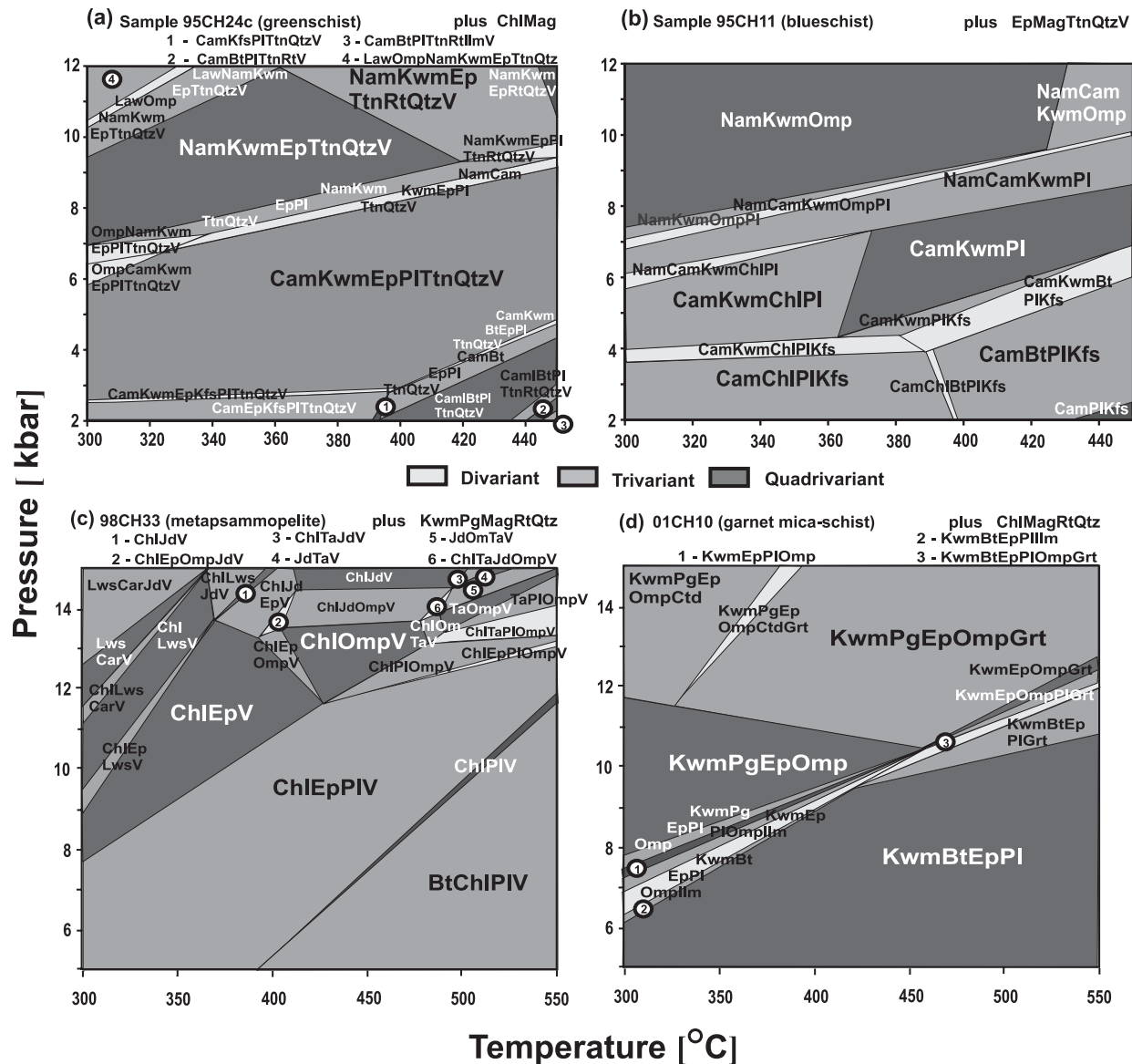
Fig. 7. *P–T* pseudosections calculated for representative whole-rock metabasite and metapsammopelite compositions (Table 2) in the system SiO_2–TiO_2–Al_2O_3–Fe_2O_3–FeO–MgO–CaO–Na_2O–K_2O–H_2O. Thermodynamic data and activity models are given in Table 3. Abbreviations not following Kretz (1983) are: Kwm, K-white mica; Nam, Na-amphibole; Cam, Ca-amphibole; V, vapour.

apatite. Cordierite (X_{Mg} 0·55–0·58, Na 0·06–0·11 a.p.f.u., Mn 0·007–0·015 a.p.f.u) with inclusions of biotite and fibrolite is intergrown with quartz and plagioclase. Two generations of sillimanite are present. Fibrolite forms prominent unoriented nodes and bands replacing biotite at its contact. Prismatic sillimanite (0·5 mm) replacing fibrolite and biotite form aggregates of centimetre size. Ti-rich biotite grains (0·2–1 mm; X_{Mg} 0·38–0·45, Ti 0·13–0·21 a.p.f.u.) grew entirely unoriented. Local late retrograde muscovite grew across sillimanite. The gneiss contains local migmatitic leucosomes of granitic composition.

METAMORPHIC EVOLUTION OF THE WESTERN SERIES
Phase relationships and reaction history

To visualize the approximate *PT* stability fields of the high variance blueschist- and greenschist-facies assemblages, pseudosections were calculated in the system K_2O–Na_2O–CaO–TiO_2–Fe_2O_3–FeO–MgO–Al_2O_3–SiO_2–H_2O from the whole-rock composition of four representative white mica-bearing samples of all major rock types (Fig. 7; Table 2). For calculating the equilibrium assemblages and respective mineral compositions,

Table 2: Whole-rock compositions of representative samples used to calculate pseudosections in Fig. 7

	95CH24c	95CH11	98CH33	01CH10
wt %				
SiO_2	46·50	47·71	61·92	53·12
TiO_2	2·53	1·89	0·87	1·04
Al_2O_3	13·34	13·70	18·04	17·26
Fe_2O_3	4·46	9·79	2·99	4·51
FeO	9·65	3·21	3·10	4·96
MgO	7·59	5·18	2·12	4·39
CaO	5·71	11·24	0·20	5·62
Na_2O	3·83	2·51	3·08	1·56
K_2O	0·07	1·37	3·22	2·12
H_2O	4·14	2·81	3·52	3·65
Sum	99·09	100·09	99·28	98·62

the Gibbs free energy minimization procedure was applied using the DEKAP code developed by Gerya *et al.* (2001). This approach is based on an algorithm suggested by de Capitani & Brown (1987). The calculation of the petrogenetic grid was performed with a resolution of 5 K and 100 bar for T and P, respectively. Calculations involved the entire thermodynamic data set for minerals and aqueous fluids of Holland & Powell (1998*a*). References to the mixing models used, consistent with this dataset, are listed in Table 3.

In the two calculated pseudosections of the blueschist and greenschist samples, which have no marked bulk-rock chemical differences, a narrow transitional field, of similar size, with coexisting Ca- and Na-amphiboles, is predicted between the blueschist and greenschist assemblages between 300°C, ~5–7 kbar and 400°C, 6–8·5 kbar (Fig. 7a and b). The predicted coexistence of two amphiboles contrasts with the observation made above that a complete compositional transition exists between Na- and Ca-amphiboles within the studied samples. The transition between the facies stability fields is actually represented by the NaCa-amphiboles winchite and barroisite, which are common in all metabasites. Hence the predicted coexistence of two amphiboles in the pseudosections must be due to the activity models used for amphibole, which imply a too wide miscibility gap. Nevertheless, the minimum pressure for blueschist assemblages at 7·8–8·8 kbar, 300–400°C is equivalent in both pseudosections. This predicts that there is a pressure difference between the recorded peak assemblages of the blueschist and greenschist samples. Lawsonite is not observed in our samples, but appears at pressures above 9–11 kbar at 300–350°C. This can be taken as a lower temperature limit for the studied epidote blueschist-facies

assemblages. At the highest temperature limit, a transitional field to the albite amphibolite facies may already appear at 430°C. In the greenschist assemblages biotite would be stable at $T > 400$°C and $P < 4$–5 kbar.
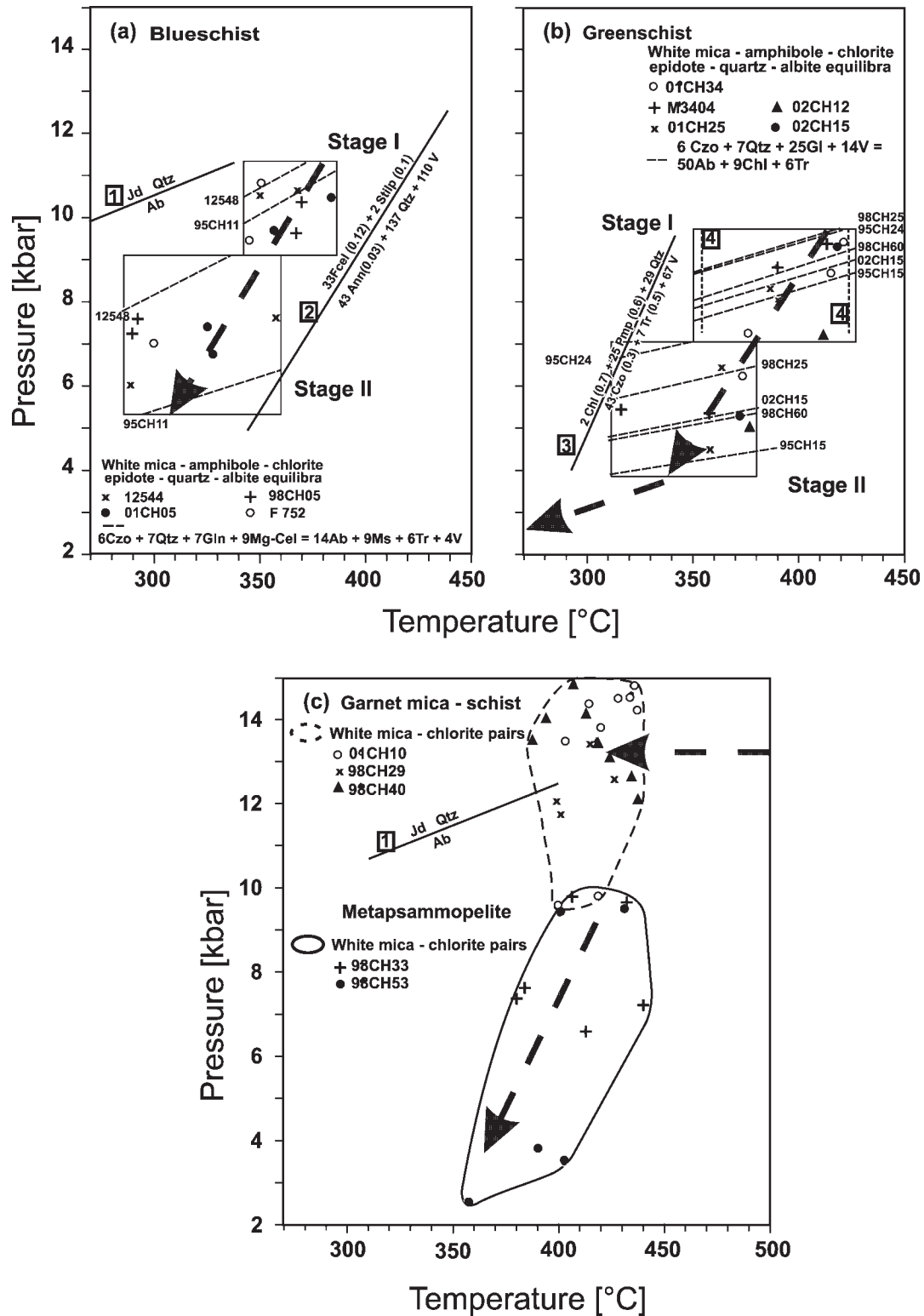
A typical pseudosection for the metapsammopelites (Fig. 7c) shows that their common assemblage white mica–chlorite–quartz–albite $\pm$ epidote is stable over a very wide PT field including greenschist, epidote blueschist and albite–epidote amphibolite facies. Lawsonite is predicted already at 9–11 kbar and 300–350°C, representing a good lower temperature limit. Garnet in the Western Series is restricted only to very Mn-rich assemblages, such as the ferruginous metasediments, and it is thus stabilized to low temperature by high Mn contents. An exception is the Ca-rich garnet mica-schist of Punta Sirena, where garnet is predicted to be stable above 10–11 kbar. However, in the absence of omphacite, temperatures should have exceeded ~450–500°C (Fig. 7d). The calculated composition of the high-pressure garnet (e.g. at 11 kbar, 550°C: almandine$_{0·661}$, grossular$_{0·241}$, pyrope$_{0·098}$) corresponds well to the measured one, as noted above.

Four localities of ferruginous metasediments (associated with blueschist and greenschist) contain the assemblage stilpnomelane–white mica (Fig. 1), proving that temperatures did not exceed stilpnomelane breakdown to biotite coexisting with phengite and quartz (Massonne & Szpurka 1997; here calculated for mean compositions; method I, Table 3) at ~350–400°C, >5 kbar (Fig. 8a). On the other hand, thorough recrystallization of quartz within the pentratively deformed rocks, lacking any visible distinction between clastic and recrystallized grains in the metapsammopelites, indicates minimum temperatures above 350°C (Brix *et al.*, 2002). The pumpellyite breakdown reaction marking the boundary between pumpellyite–actinolite and greenschist facies (Evans, 1990; here calculated for mean compositions; method I, Table 3) at 300–350°C, >5 kbar (Fig. 8b), was well overstepped in the entire study area. Also, retrograde pumpellyite did not form, indicating that retrograde metamorphic reactions appear to have ceased before cooling through 300°C. Hence the evolution of most rocks of the study area was apparently restricted to a rather narrow temperature range. Maximum pressure is limited by the presence of pure albite in all rock types to below 10·5–12·5 kbar at 300–400°C.

The reaction history leading to the omnipresent, conspicuous, retrograde zoning in amphibole and other hydrous phases (white mica, chlorite, epidote) appears to be governed by the presence of a free interstitial hydrous fluid phase. Abundant growth of postkinematic late albite porphyroblasts and different generations of late quartz-filled veins cutting the pervasive foliation are visible expressions of the presence of free fluids on the entire retrograde path. However, it is questionable if an external

Table 3: References for thermodynamic data and activity models used for the various geothermobarometric approaches

Mineral	Components	End-member data	Activity formulation
For calculation of the pseudosections			
Clinopyroxene	jadeite, diopside, hedenbergite, omphacite	Holland & Powell (1998*a*)	Vinograd (2002*a*, 2002*b*)
Na-amphibole	glaucophane, tremolite, tschermakite, Fe-glaucophane	Holland & Powell (1998*a*)	Will *et al.* (1998)
Ca-amphibole	glaucophane, tremolite, tschermakite, Fe-actinolite, pargasite	Holland & Powell (1998*a*)	Dale *et al.* (2000)
Paragonite	paragonite, margarite	Holland & Powell (1998*a*)	Will *et al.* (1998)
K-white mica	muscovite, Mg−Al-celadonite, Fe−Al-celadonite, paragonite	Holland & Powell (1998*a*)	Powell & Holland (1999)
Biotite	annite, phlogopite, eastonite, ordered biotite	Holland & Powell (1998*a*)	Powell & Holland (1999)
Chlorite	clinochlore, daphnite, Mg-amesite, Al-free chlorite	Holland & Powell (1998*a*)	Holland & Powell (1998*b*)
Plagioclase	anorthite, albite	Holland & Powell (1998*a*)	Will *et al.* (1998)
Epidote	clinozoisite, epidote, Fe-epidote	Holland & Powell (1998*a*)	
Rutile, titanite, quartz magnetite, lawsonite, K-feldspar		Holland & Powell (1998*a*)	$a = 1$
For calculation of the multivariant reactions			
Method 1			
Amphibole	glaucophane	Evans (1990)	Massonne (1995*a*, 1995*b*)
	tremolite	Berman (1988)	Massonne (1995*a*, 1995*b*)
Chlorite	clinochlore	Massonne (1995*b*)	Massonne (1995*a*)
	daphnite	Massonne & Szpurka (1997)	as Massonne (1995*a*)
Epidote	clinozoisite	Berman (1988)	Berman (1988), $a_{\text{Clinozoisite}} = 1 - X_{\text{Pistazite}}$
Garnet	grossular	Berman (1990)	Berman (1990)
	pyrope	Berman (1990)	Berman (1990)
	almandine	Berman (1990)	Berman (1990)
K-white mica	muscovite	Massonne (1997); Massonne & Szpurka (1997)	Massonne (1997)
	Mg−Al-celadonite	Massonne (1995*b*)	Massonne (1995*b*, 1997)
	Fe−Al-celadonite	Massonne (1995*b*)	Massonne (1995*b*, 1997)
Biotite	phlogopite	Berman (1988)	McMullin *et al.* (1991)
	annite	Berman (1990)	McMullin *et al.* (1991)
Pumpellyite	Mg-pumpellyite	Evans (1990)	Evans (1990)
Stilpnomelane	stilpnomelane	Massonne & Szpurka (1997)	Massonne & Szpurka (1997)
Plagioclase	albite	Berman (1988)	$a_{\text{albite}} = X_{\text{albite}}$
Quartz		Berman (1988)	
K-feldspar		Berman (1988)	
Method 2			
Chlorite	clinochlore	Vidal *et al.* (2001)	Vidal *et al.* (2001)
	daphnite	Vidal *et al.* (2001)	Vidal *et al.* (2001)
	Mg-amesite	Vidal *et al.* (2001)	Vidal *et al.* (2001)
K-white mica	muscovite	Parra *et al.* (2002*a*, 2002*b*)	Parra *et al.* (2002*a*, 2002*b*)
	Mg−Al-celadonite	Parra *et al.* (2002*a*, 2002*b*)	Parra *et al.* (2002*a*, 2002*b*)
	Fe−Al-celadonite	Parra *et al.* (2002*a*, 2002*b*)	Parra *et al.* (2002*a*, 2002*b*)

Fig. 8. *PT* estimates and partial *PT* paths for rocks of the Western Series (blueschist, greenschist, garnet mica-schist, metapsammopelite). Numbered reactions are as follows: (1), upper stability of albite after Holland (1980); (2), (3), reactions calculated with average compositions (method 1; Table 3): (4), garnet–amphibole thermometry (Fe-metasediments). Reactions and invariant points for blueschist and greenschist were calculated with method 1; those for metapsammopelite and garnet mica-schist with method 2 (Table 3). Grey arrows indicate the direction of the *PT* path; boxes mark the range of *PT* results for stages I and II.

fluid influx is necessary for retrograde reaction progress, considering the common assumption that water released during prograde dehydration left the system. Pressure-sensitive multivariant reactions such as reaction (E6) (see Table 4) at the blueschist–greenschist-facies transition, that are used for geobarometry below, have water partly as a reactant on the high-pressure side, but also on the low-pressure side [see reaction (5), Table 4]. This means that water can be consumed or released during continuous retrograde decompression reactions. The calculated pseudosections allow quantification of the change in the amount of free water relative to the bulk water content of the system with changing *PT* conditions (Fig. 9), assuming that reactions are instantaneous and complete, and the water content of the rock was the total water content of the system. Considering *PT* changes from 400°C, 8–10 kbar to 350°C, 5 kbar (simulating the partial *PT* path derived above) the changes in $X_{\text{free water}}/X_{\text{bulk water}}$ are negative for greenschist sample 95CH24 (consumption of free water), but positive for blueschist sample 95CH11 and the metapsammopelitic sample 98CH32 (release of free water). This predicts that with continuous reaction during decompression at low-grade conditions (either isothermally or with slight cooling), the amount of free water might increase in many cases, such that no external water is required for reactions to proceed. A limited amount of steadily available free water will favour localized equilibrium over short distances during continuous mineral growth with activities of elements in the fluid always buffered.

Geothermobarometry

For quantification of the *PT* conditions for equilibration stages along the *PT* path, local equilibria with multivariant reactions were calculated using mineral compositions of phases in close contact. Multivariant equilibria calculations were undertaken mainly using the Ge0calc software of Brown *et al.* (1989) and derivations (TWQ) with the thermodynamic dataset of Berman (1988) supplemented by further compatible data and activity models (Table 3). A list of the calculated reactions is given in Table 4. Results are plotted in Fig. 8.

Metabasite

Because of the high number of reliable components available for calculations, good geothermobarometric results were obtained for the low-variance assemblage amphibole–white mica–chlorite–epidote–quartz–albite. Invariant points were calculated using the water-independent multivariant reactions (E1)–(E4) (Table 3). Including water as a further phase, nine additional reactions were calculated. However, these relatively flat water-dependent reactions are not only sensitive to minor changes in (unknown) water activity, but also are much more dependent on the activity of the clinozoisite component than the water-independent ones. Thus their use as a further check for equilibrium conditions is limited, although closest coincidence of all possible invariant points was always approached. For blueschist samples lacking chlorite, the water-dependent reaction (E5) was used as a barometer; for greenschist lacking white mica, the water-dependent reaction (E6) was calculated.

The two generations of amphibole in the two different metabasite rock types reflect two stages of equilibration along a partial *PT* path, a peak metamorphic stage I and a retrograde stage II. Calculations of the stage I conditions yield a range of *PT* results (invariant points) of 9·5–10·7 kbar, 350–385°C for the blueschist and 7·0–9·3 kbar, 380–420°C for the greenschist (Fig. 8). The temperature range for the latter was independently corroborated by conventional Fe–Mg exchange thermometry with rims of garnet–amphibole pairs (Graham & Powell, 1984) in two magnetite–stilpnomelane rocks (samples 95CH25 and 98CH25). The scatter presumably represents continuous equilibration around peak *PT* conditions during the late prograde and early retrograde *PT* path, which could not be resolved in detail in the present case, but also differences in peak pressure between greenschist samples are likely. Calculations of the stage II conditions yielded a range of *PT* results of 6·0–7·7 kbar, 290–345°C for the blueschist and 4·4–7·2 kbar, 315–380°C for the greenschist (Fig. 8), thus indicating pressure release with slight cooling. The slight temperature difference between the paths of the blueschist and greenschist presumably concurs with a generally higher Tschermaks substitution in the amphiboles of the greenschist (Fig. 3c).

There is no regional trend in the distribution of peak pressures (Fig. 1), but there is a significant peak pressure difference between the two metabasite types as predicted from the pseudosections. It is often argued that in the Chilean basement the very rare blueschist assemblages are the principal relics of HP–HT conditions generally completely erased by a pervasive retrograde greenschist overprint (e.g. Kato, 1985; Martin *et al.*, 1999). Here peak *PT* compositions of solid-solution phases are regarded as preserved in most rock types for the following reasons:

(1) relic magmatic clinopyroxene phenocrysts are replaced by Na-, CaNa- or Ca-amphibole in different rock types. It seems unlikely that a premetamorphic phase is preserved but not the peak metamorphic amphibole.

(2) A pervasive overprint, erasing all relic compositions, could be driven by influx of abundant external fluid; however, this should lead to phase reduction. Such metasomatic effects are frequently observed, but not predominant in the metabasite lenses, where low-variance assemblages are also common. It was shown above that

Table 4: List of calculated multivariant reactions

(E1)	6 clinozoisite$_{ep}$ + 7 quartz + 11 glaucophane$_{amp}$ + 10 Fe−Al-celadonite$_{wm}$ = 22 albite + 3 Mg−Al-celadonite$_{wm}$ + 2 daphnite$_{chl}$ + 7 muscovite$_{wm}$ + 6 tremolite$_{amp}$
(E2)	6 clinozoisite$_{ep}$ + 7 quartz + 11 glaucophane$_{amp}$ + 7 Mg−Al-celadonite$_{wm}$ = 22 albite + 2 clinochlore$_{chl}$ + 7 muscovite$_{wm}$ + 6 tremolite$_{amp}$
(E3)	daphnite$_{chl}$ + 5 Mg−Al-celadonite$_{wm}$ = 5 Fe−Al-celadonite$_{wm}$ + clinochlore$_{chl}$
(E4)	30 clinozoisite$_{ep}$ + 35 quartz + 55 glaucophane$_{amp}$ + 35 Fe−Al-celadonite$_{wm}$ = 110 albite + 7 daphnite$_{chl}$ + 3 clinochlore$_{chl}$ + 35 muscovite$_{wm}$ + 30 tremolite$_{amp}$
(E5)	6 clinozoisite$_{ep}$ + 7 quartz + 7 glaucophane$_{amp}$ + 9 Mg−Al-celadonite$_{wm}$ = 14 albite + 9 muscovite$_{wm}$ + 6 tremolite$_{amp}$ + 4 H$_2$O
(E6)	6 clinozoisite$_{ep}$ + 7 quartz + 25 glaucophane$_{amp}$ + 14 H$_2$O = 50 albite + 9 clinochlore$_{chl}$ + 6 tremolite$_{amp}$
(E7)	4 Mg−Al-celadonite$_{wm}$ + daphnite$_{chl}$ + muscovite$_{wm}$ = Mg-amesite$_{chl}$ + 5 Fe−Al-celadonite$_{wm}$
(E8)	5 Fe−Al-celadonite$_{wm}$ + 5 Mg-amesite$_{chl}$ = 5 muscovite$_{wm}$ + 4 clinochlore$_{chl}$ + daphnite$_{chl}$
(E9)	Mg−Al-celadonite$_{wm}$ + Mg-amesite$_{chl}$ = muscovite$_{wm}$ + clinochlore$_{chl}$
(E10)	clinochlore$_{chl}$ + 4 Al-celadonite$_{wm}$ = muscovite$_{wm}$ + 3 phlogopite$_{bt}$ + 7 quartz + 4 H$_2$O
(E11)	3 Mg−Al-celadonite$_{wm}$ = phlogopite$_{bt}$ + 2 K-feldspar + 3 quartz + 2 H$_2$O
(E12)	phlogopite$_{bt}$ + almandine$_{grt}$ = annite$_{bt}$ + pyrope$_{grt}$
(E13)	pyrope$_{grt}$ + grossular$_{grt}$ + muscovite$_{wm}$ = 3 anorthite$_{pl}$ + phlogopite$_{bt}$
(E14)	almandine$_{grt}$ + grossular$_{grt}$ + muscovite$_{wm}$ = 3 anorthite$_{pl}$ + annite$_{bt}$
(E15)	grossular$_{grt}$ + quartz + 2 sillimanite = 2 anorthite$_{pl}$
(E16)	2 almandine$_{grt}$ + 2 phlogopite$_{bt}$ + 5 quartz + 4 sillimanite = 3 Mg-cordierite$_{crd}$ + 2 annite$_{bt}$
(E17)	2 pyrope$_{grt}$ + 5 quartz + 4 sillimanite = 3 Mg-cordierite$_{crd}$
(E18)	2 almandine$_{grt}$ + 6 anorthite$_{pl}$ + 2 phlogopite$_{bt}$ + 3 quartz = 3 Mg-cordierite$_{crd}$ + 2 grossular$_{grt}$ + 2 annite$_{bt}$
(E19)	3 Mg-cordierite$_{crd}$ + 5 grossular$_{grt}$ + 4 sillimanite = 2 pyrope$_{grt}$ + 15 anorthite$_{pl}$
(E20)	6 anorthite$_{pl}$ + 2 pyrope$_{grt}$ + 3 quartz = 2 grossular$_{grt}$ + 3 Mg-cordierite$_{crd}$

major external fluid infiltration is unlikely for most of the studied rocks.

Metapsammopelite

For the high-variance assemblage present in most of the metapsammopelitic rocks, thus far only the approach of Vidal & Parra (2000) and Parra *et al.* (2002a, 2002b), using coexisting chlorite–phengite equilibria, has been shown to yield consistent results, especially for metapelites in similar HP–LT terranes. This approach (method 2; Table 3) is based on thermodynamic solution models involving the Tschermak and pyrophyllitic substitutions in white mica and the di/trioctahedral substitution in chlorite. Application of this approach to the metapsammopelitic rocks of the study area is, however, restricted only to the water-independent multivariant equilibria (E7)–(E9) and (E3). All analysed iron is assumed to be ferrous in this approach. Other possible end-members with contents in chlorite and mica of less than 5% (e.g. sudoite, pyrophyllite) could not be considered because of the high uncertainty of their activity in these phases. For two metapsammopelitic schist samples calculated ranges of conditions of local equilibria of 4–9·6 kbar, 355–435°C suggest similar peak *PT* conditions and decompressional overprint to those in the greenschists. Hence a comparable *PT* evolution path for both rock types is inferred (Fig. 8b and c).

In contrast, the garnet mica-schist yields deviating results. Multiple tests with available multivariant reactions and conventional thermometers involving garnet do not yield any reasonable results, and show that garnet is not in equilibrium with white mica or chlorite. This concurs with the observation that chlorite, white mica and epidote replace garnet at its rims. Evidently the matrix assemblage around garnet is a second retrograde one. Phengite inclusions in garnet, albite and titanite have different compositions than matrix white micas and are prograde. Considering the results from the pseudosections, $P > 10$–11 kbar and $T > \sim 450$–500°C must have been realized to produce the garnet during an older, higher temperature stage I. Chlorite–phengite equilibria of coexisting pairs in the matrix indicate conditions of 390–440°C, 9·6–14·7 kbar (method 2; Table 3). The conditions of this retrograde stage II partly appear to be at too high pressure, because the upper stability of albite should have been overstepped and no jadeite is observed. Nevertheless, they still indicate significantly higher *PT* conditions than in the metapsammopelites and the greenschist of the study area (Fig. 8). The relation between stages I and II suggests an isobaric cooling path at ∼12–13 kbar. The garnet mica-schist is very similar to a garnet mica-schist associated with a garnet amphibolite in the Western Series of south–central Chile (Willner *et al.*, 2004b), which yielded an anticlockwise *PT* path and highest
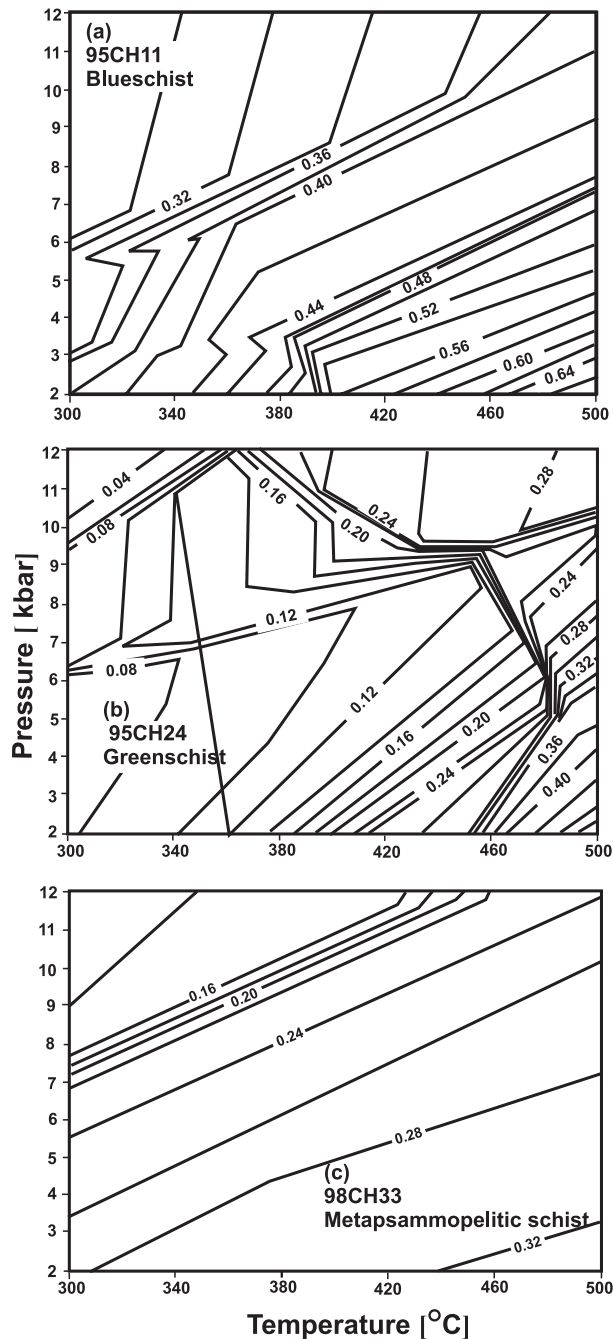
Fig. 9. *P–T* maps showing isolines of calculated ratios $X_{\text{free } H_2O}/X_{\text{total } H_2O}$ in assemblages calculated from whole-rock analyses (see pseudosections in Fig. 7).

regional *PT* conditions. This similarity corroborates the unusual evolution of the garnet mica-schist. Similar to the analogue from south–central Chile, the garnet mica-schist studied here also yields an age related to stage II that is significantly older than the ages of the peak of metamorphism in the area (Willner *et al.*, 2005).

METAMORPHIC EVOLUTION OF THE EASTERN SERIES

The interpretation of the HT metamorphic sequence and phase relationships in the Eastern Series is straight-forward (Fig. 10). The zonation and sequence of mapped assemblages indicate progressive increase in grade from upper greenschist facies to granulite facies, suggesting a classic 'Abakuma-type' sequence at pressures below the aluminosilicate triple point. The sequence starts with the formation of biotite, passes the staurolite-in reaction in the andalusite stability field and the staurolite–quartz–muscovite-out reaction in the sillimanite stability field, and ends with the first anatectic melts. Breakdown of muscovite + quartz in the sillimanite field before reaching the wet granite solidus indicates a pressure below 3·6 kbar (intersection of the muscovite + quartz breakdown and wet granite solidus curves). This is consistent with the position of the univariant reaction Bt + Sil + Qtz = Grt + Cord + Kfs + H_2O of the KFMASH system (Spear & Cheney 1989), which is recorded by the highest grade assemblage.

Geothermobarometry is consistent with predictions from the petrogenetic net (Fig. 10). All calculations were carried out using method 1 (Table 3) with multivariant reactions (E10)–(E20) listed in Table 4. In the biotite zone, the temperature can be approximated calculating reaction (E10) (curve 3a in Fig. 10) and the minimum pressure with reaction (E11) (curve 3b in Fig. 10) involving a theoretical K-feldspar. For mica-schist 01CH29 approximate conditions of 2–3 kbar, 400–450°C result. *PT* conditions in the medium-grade rocks can be estimated in two ways. (1) Overstepping the staurolite-in reaction conditions in the andalusite stability field requires ∼520–580°C, 2·5–3 kbar around the isopleth $X_{\text{Fe}} = 0·9$ for garnet coexisting with staurolite, biotite, muscovite and quartz (Spear & Cheney 1989; curve 4 in Fig. 10). (2) Invariant point 5 in Fig. 10 was calculated on the basis of the three water-independent reactions (E12)–(E14). For sample 01CH42, conditions of 555°C, 3·2 kbar result.

Evaluation of the highest grade conditions are as follows: (1) Fe–Mg exchange thermometry for cordierite–biotite pairs (Bhattacharya *et al.*, 1988) in sample 01CH48 results in 684–716°C (point 8 in Fig. 10), and the isopleth $X_{\text{Fe}} = 0·85$ for garnet coexisting with cordierite, biotite, K-feldspar and quartz occurs at 650°C (curve 7 in Fig. 10). The position of the univariant reaction Bt + Sil + Qtz = Grt + Cord + Kfs + H_2O in this temperature range indicates a minimum of 2·5–3·2 kbar. (2) An invariant point (point 6 in Fig. 10) was calculated intersecting seven multivariant water-independent reactions [(E15)–(E20), (E12)] including coexisting cordierite, biotite, garnet, quartz, sillimanite and plagioclase. For sample 01CH48 peak conditions at 690°C, 3·45 kbar
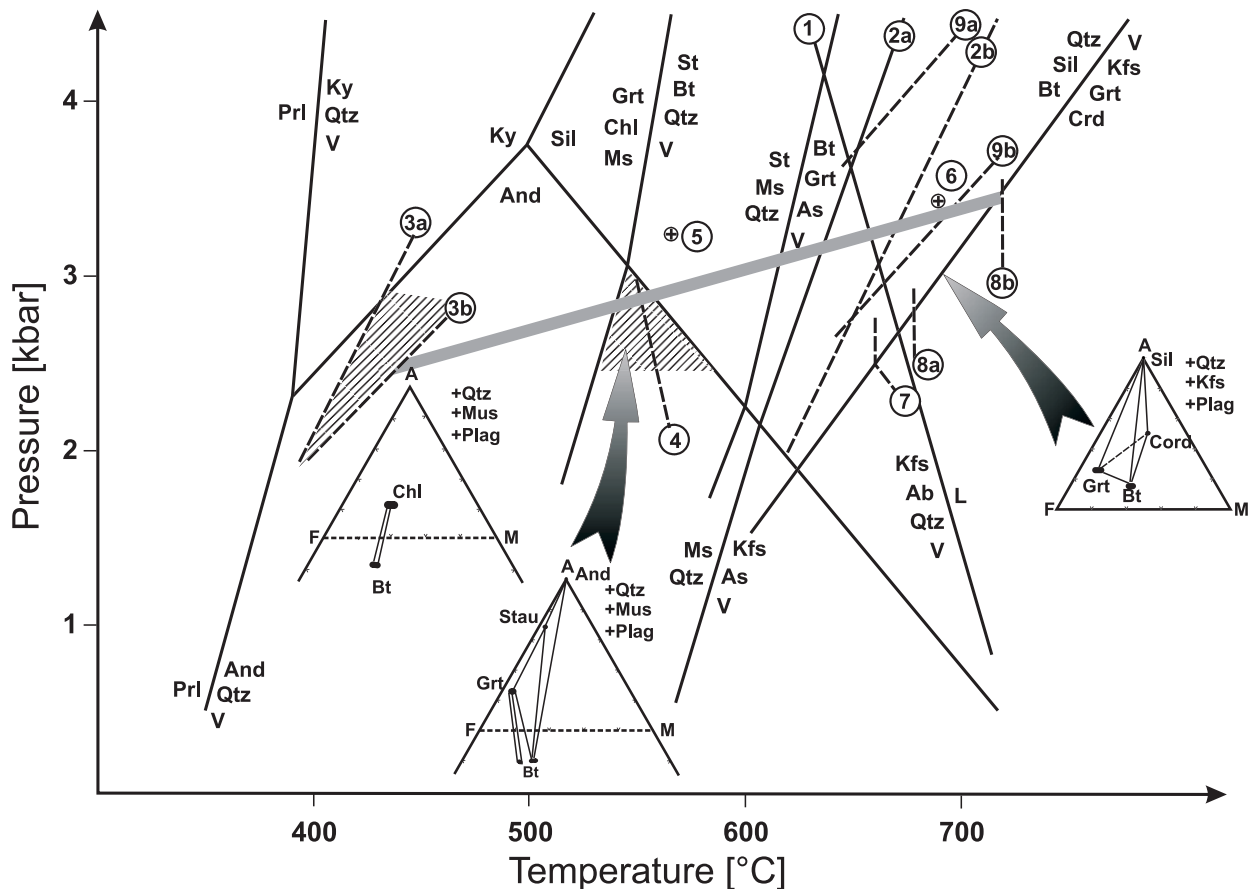
Fig. 10. Petrogenetic grid for rocks of the Eastern Series. The approximate range of *PT* variation is indicated by the grey bar. Unnumbered curves are from Spear & Cheney (1989). Numbered curves are as follows: 1, Johannes (1984); 2a, calculated for pure phases; 2b, calculated for muscovite with Si 3·06 a.p.f.u.; 3a, 3b, reactions (E10) and (E11), respectively, calculated for compositions in sample 01CH29; 4, $X_{Fe} = 0.9$ in garnet coexisting with staurolite, biotite, quartz and muscovite (Spear & Cheney 1989); 5, calculated invariant point [reactions (E12)–(E14) in Table 4] for the assemblage garnet–muscovite–biotite–quartz in sample 01CH43; 6, calculated invariant point [reactions (E12), (E15)–(E20); Table 4] for the assemblage garnet–cordierite–biotite–sillimanite–plagioclase–K-feldspar–quartz in sample 01CH48; 7, $X_{Fe} = 0.85$ in garnet in assemblage with cordierite, biotite, quartz and K-feldspar (Spear & Cheney 1989); 8a, 8b, Fe–Mg exchange thermometer for garnet–cordierite in sample 01CH43; 9a, calculated Si 3·08 a.p.f.u. isopleth, and 9b, Si 3·04 a.p.f.u. isopleth for muscovite coexisting with biotite, K-feldspar and quartz [reaction (E11) in Table 4]. Measured mineral compositions are plotted in the inset AFM projections.

result. Using water-dependent multivariant reactions including the same components as well as K-feldspar (nine reactions), a reduced water activity can be estimated at ∼0·5.

The intrusion depth of the neighbouring granite (98CH43) was approximated using the zoned magmatic muscovite coexisting with biotite and K-feldspar. Intersection of reaction (E11) with the wet granite solidus is at 3·6 kbar for an Si content of 3·08 a.p.f.u. in white mica cores (curve 9a in Fig. 10) and at 2·8 kbar for Si 3·04 a.p.f.u. in the white mica rims (curve 9b). The quartz–muscovite breakdown curve is considerably lowered for Si 3·08 a.p.f.u. (curve 2b in Fig. 10). Hence most muscovite presumably crystallized near the granite solidus just on the low-temperature side of the muscovite + quartz breakdown curve.

DISCUSSION AND GEODYNAMIC CONSTRAINTS

The petrological information derived in this study from the paired metamorphic belt can contribute to a tentative reconstruction of the approximate thermal structure of the former continental margin and its geometric constraints. The resulting conceptual model is presented in Fig. 11.

The evolution of the accretionary prism

The protoliths of the metabasites and metapsammo-pelites in the Western Series are of very different origin; that is, from the uppermost part of the subducting oceanic plate and predominantly from the overriding continental plate (terrigeneous trench filling), respectively.
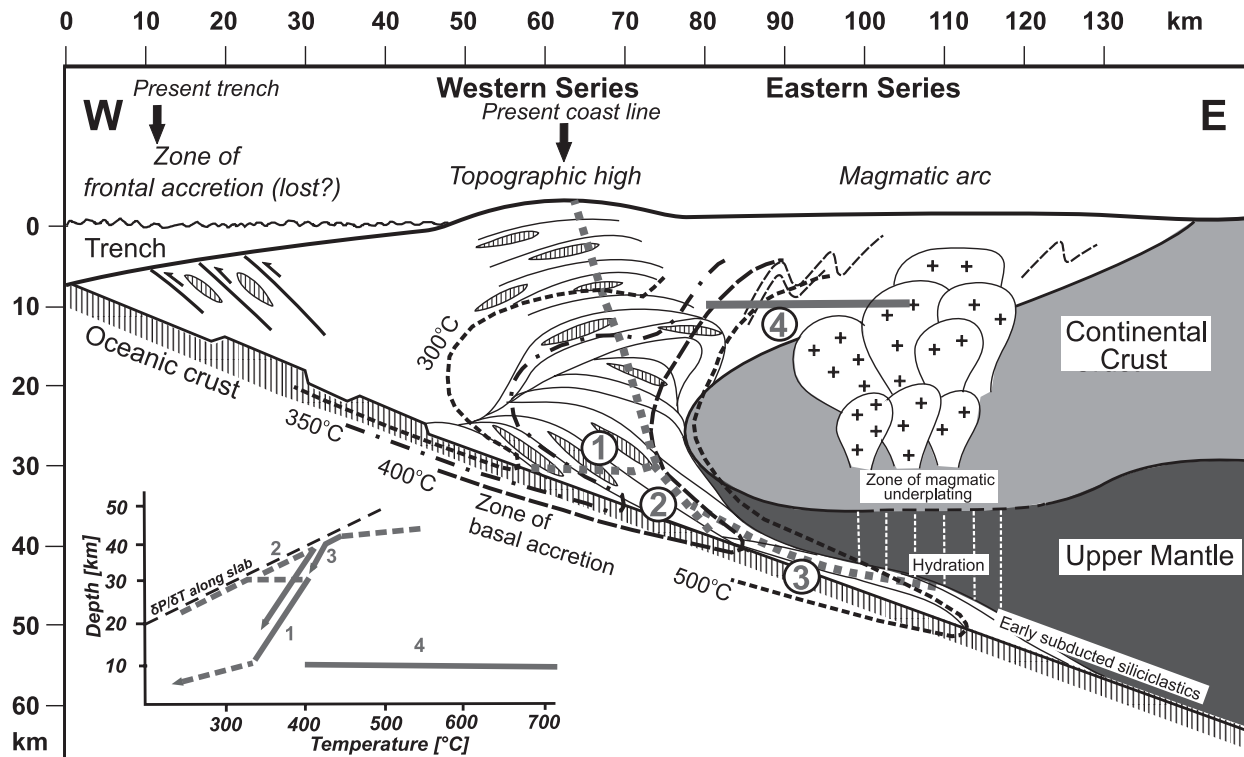
Fig. 11. Conceptual model of the convergent margin of central Chile during late Palaeozoic times. Grey lines in the figure and the depth–temperature inset (summary of Figs 8 and 10) indicate tentative particle and depth–temperature paths in the Western Series of: 1, greenschist; 2, blueschist; 3, garnet mica-schist; line 4 represents the level of isobaric heating and cooling in the Eastern Series. Black dashed lines are isotherms.

Nevertheless, it can be shown that their metamorphic evolution, their deformational history and their metamorphic ages (Willner *et al.*, 2005) are similar, which indicates a joint evolution from the earliest detectable stage. Their mixture could have occurred during subduction and early basal accretion. Analogue modelling by Gutscher *et al.* (1998) has demonstrated that effective subduction of long, thick sheets of sediments is possible with high basal friction during low-angle subduction involving steep erosional frontal slopes. As shown above, the oceanic crust incorporated into the Western Series may also have included alkali basalts. Thus a decrease of the subduction angle (or even resistance to subduction) might have been caused by the presence of oceanic islands on the subducting slab.

Peak *PT* conditions of the greenschists (7·0–9·3 kbar, 380–420°C) indicate metamorphism under a metamorphic gradient of 11–16°C/km (on the basis of an average density of 2·8 g/cm^3), which appears relatively high for a subduction environment. However, this gradient seems to be typical for the Western Series as it was also detected in south–central and southern Chile (Willner *et al.*, 2000, 2001). The elevated metamorphic gradient may be due to several factors. Numerical modelling by Peacock (1996) predicts that (1) slow subduction and (2) a relatively flat subducting slab may enhance

the thermal gradient. (3) The subduction of upper crustal material (greywackes) with high contents of radiogenic elements also contributes to the heat production at depth. A further factor (4) is envisaged here: analogue modelling has recently shown that basal accretion during flat subduction may involve formation of long, flat duplexes forming an antiformal stack (Kukowski *et al.*, 2002). This is tentatively included in the conceptual model (Fig. 11). Such a process predicts that part of the accreted material will initially move horizontally away from the lower plate before vertical exhumation and thus cross isotherms towards higher temperatures at maximum depth. A near-isobaric, late, prograde *PT* path (particle path 1 in Fig. 11) can be expected, although it could not be deduced for the studied rocks. However, a late prograde heating with little pressure variation is known from albite amphibolite grade rocks of comparable settings (Chonos Archipelago–Chile: Willner *et al.*, 2000; South Shetland Islands: Trouw *et al.*, 1998). A pervasive subhorizontal foliation (s_2, locally s_3) mainly originated during peak *PT* conditions, reflecting basal accretion and crustal thinning at depth following basal accretion.

The occurrence of glaucophane-bearing blueschist must be considered as extremely rare, because only three localities are known along the ~1500 km of basement exposure of the Coastal Cordillera (Willner *et al.*,

2004a, 2004b) implying a special preservation mode. This rock was metamorphosed to significantly different peak PT conditions at 9·5–10·7 kbar, 350–385°C, corresponding to a lower metamorphic gradient ($\sim$9–11°C/km) than in the predominant greenschist. There is no difference in peak PT ages of both neighbouring metabasite types (Willner et al., 2005). This appears problematic, because a higher peak temperature would be expected for the blueschists compared with the greenschists if they were metamorphosed along a gradient parallel to the subducting slab (Fig. 11). More common metabasites, which were subducted to similar depths as the blueschists in other areas of the Western Series, are metamorphosed to albite–epidote–amphibolite facies (Kato, 1985; Trouw et al., 1998; Willner et al., 2000, 2004a), showing comparable metamorphic gradients to the greenschists. Here it is suggested that the blueschists were derived from the lowermost part of the basal accretion zone of the accretionary wedge, near the uppermost tip of the mantle wedge (Fig. 11; particle path 2), and that they conserved the original thermal gradient along the subducting slab (see Fig. 11), as was also implied by Trouw et al. (1998) and Willner et al. (2004a, 2004b) for similar settings containing blueschists. However, the blueschists were not heated during exhumation. It is suggested that they were emplaced by local low-angle thrusting at depth onto the already isobarically heated greenschists.

The second 'exotic' rock type is the unusual garnet mica-schist at Punta Sirena that yielded the highest PT conditions in the entire study area (390–440°C, 9·6–14·7 kbar), which were shown to reflect a retrograde stage after presumable isobaric cooling from a still higher peak temperature (particle path 3 in Fig. 11). The ages for this stage are the oldest recorded in the study area (Willner et al., 2005). A geodynamic interpretation can be provided by analogy to a better constrained occurrence in south–central Chile (Willner et al., 2004b), to similar findings in comparable settings worldwide (e.g. Wakabayashi, 1990), and to numerical modelling (Gerya et al., 2003). Siliciclastic material was subducted at the earliest stage of accretion to the deepest level under the mantle wedge and heated in contact with a still hot mantle. Later accreted material at this site caused hydration and cooling of the earliest accreted material and the overlying mantle. After this change (also of rheological conditions in the mantle), effective exhumation of the early subducted material followed at the base of the hydrated mantle wedge within a cooler environment than during its burial. The exotic garnet mica-schist thus provides an important relic and time marker for the onset of subduction mass flow in the Coastal Cordillera accretionary prism. It must be noted that its predominant retrograde equilibration occurred under the same metamorphic gradient as the blueschist, presumably in a position near the subducting slab (Fig. 11).

In all rock types of the Western Series a similar type of partial exhumation path, involving slight cooling with decompression, is preserved that is also similar to those of other HP–LT belts worldwide (e.g. Vidal & Parra, 2000, and references therein). It involves decompression with only slight cooling after peak metamorphic conditions recorded by the formation of retrograde local equilibria in the presence of free water and crystallization–recrystallization processes. The retrograde overprint occurred within a narrow temperature range of 300–400°C. Continuous reactions during pressure release of $\sim$3–4 kbar caused further crystal growth at the rims, as well as recrystallization, recording a clockwise decompression path. Further reaction to below 300°C is probably hampered for kinetic reasons. The geometry of the retrograde PT path implies a kink after cooling through 350°C at $\sim$4 kbar to cooling below 300°C at $\sim$2–3 kbar (Fig. 8). Late exhumation thus occurred under a high geothermal gradient, implying a 'doming' of isotherms above the accretionary prism (Fig. 11). Retrograde mineral growth and recrystallization generally occurred under strain-free conditions. Retrograde ductile deformation is restricted to rare local shear bands, indicating that there is little tectonic control of the exhumation process.

The high-temperature belt

The spatial field relationships of isograd surfaces dipping to the west and following the north–south trend of the batholith along strike indicate a close relation to a major heat input during the intrusion of the arc batholith. The HT metamorphic overprint of regional extent in the Eastern Series involves progressively rising temperatures from 400°C to 720°C toward the intruding batholith at a uniform shallow level at $\sim$10 km depth (3 $\pm$ 0·5 kbar), which is also consistent with the intrusion depth of the batholith. It can be shown that the HT metamorphism and the main intrusion pulse of the batholith is contemporaneous at $\sim$300 Ma (Willner et al., 2005). The observed HT metamorphism involves a nearly isobaric temperature increase, which requires a short-time massive heat input related to voluminous magma emplacement. For the retrograde path, a short-term isobaric cooling occurred, at nearly the same temperature as those prevailing in the neighbouring Western Series. A lack of inverse zonation in high-temperature garnets precludes a long time of cooling. In contrast with the Western Series, the local retrograde overprint is of very low temperature type and unrelated to the early exhumation path. Although no definite metamorphic relics prior to the HT overprint of the Eastern Series were detected in the study area, deformation structures were overprinted that occur at very low grade conditions in the Eastern Series of other areas in the Coastal Cordillera basement (Hervé, 1988).

The garnet mica-schist in the Western Series could have reached its maximum depth during subduction roughly below the magmatic arc. As shown by Willner *et al.* (2005), its peak of metamorphism is older than the main pulse of intrusion in the magmatic arc. Considering the above inferred genetic model for the garnet mica-schist, it seems conceivable that some siliciclastic material was subducted to great depth at an early stage, giving rise to a pulse of hydrous fluids released by dehydration that could be responsible for generating the substantial volume of magmas of the late Palaeozoic arc.

The conceptual model

The above considerations point to a convergent subduction regime above a relatively low-angle subducting slab. The data from the study area can help to construct a conceptual model for the Early Palaeozoic convergent margin at an approximate scale (Fig. 11). According to the recorded maximum *PT* data and their link to the penetrative deformation, basal accretion occurred in the Western Series at a depth of ∼25–40 km, and small quantities of subducted material (garnet mica-schist) reached maximum depths of ∼45–50 km at an early stage. If the relationship between this deeply subducted material and the main pulse of magma formation in the arc is correct, this implies a depth of ∼45–50 km of the subducting slab just below the magmatic arc. The distance between the axis of the magmatic arc and the boundary of the Western and Eastern Series in the southern study area is ∼30 km. This boundary marks the transition between two environments of contrasting crustal thickness and exhumation rates (Willner *et al.*, 2005). It is assumed here that the thickness of the accretionary prism is a maximum (∼40 km) at this boundary. The distance of ∼30 km hence marks the horizontal distance between the slab at ∼40 km and at ∼50 km depth. A dip angle of the subducting slab of ∼25° and a width of the Western Series of ∼40 km results. Isotherms along the subducting slab were drawn in Fig. 11 according to the metamorphic gradient indicated by the blueschist and garnet mica-schist, but at lower crustal levels according to the retrograde path of all rock types and the metamorphic zonation in the Eastern Series.

The boundary between the two metamorphic units lacks an apparent shear zone juxtaposing different crustal levels and excising intermediate levels as is common in orogens worldwide. This transitional nature has been observed at several sites in the Coastal Cordillera (see Hervé, 1988). Such a special situation can be explained only by the cyclic nature of particle paths in the accretionary prism (Western Series), when continuous basal accretion at depth is mainly outbalanced by erosion of the forearc, as is also inferred by modelling (e.g. Kukowski *et al.*, 2002). This creates a stack of crustal slices from the base to the top of the crust with a similar metamorphic and deformational imprint. The retro-wedge (Eastern Series), including the magmatic arc, remained relatively stationary during accretion. Brittle thrusting of the Eastern Series on top of the Western Series, as observed in the north of the study area, occurred at an upper crustal level a long time after accretion had ceased (Willner *et al.*, 2005). This is related to late shortening of the convergent margin.

The oceanward continuation of the Western Series (i.e. the part of the prism with frontal accretion) is not observed anywhere in the Coastal Cordillera basement. However, within the offshore continuation of continental crust ∼50–80 km toward the west, relics of this missing frontal accretion zone might still be preserved. Hence, it is concluded that in the study area a nearly intact Late Palaeozoic convergent margin, including an accretionary prism and a magmatic arc, is preserved, in which continuous basal accretion of mainly siliciclastic material and minor uppermost oceanic crust occurred over a limited range of time and above a low-angle subducting slab.

SUPPLEMENTARY DATA

Supplementary data for this paper are available on *Journal of Petrology* online.

REFERENCES

Aguirre, L., Hervé, F. & Godoy, E. (1972). Distribution of metamorphic facies in Chile: an outline. *Krystallinikum* **9**, 7–19.

Berman, R. G. (1988). Internally-consistent thermodynamic data for minerals in the system Na$_2$O–K$_2$O–CaO–MgO–FeO–Fe$_2$O$_3$–Al$_2$O$_3$–SiO$_2$–TiO$_2$–H$_2$O–CO$_2$. *Journal of Petrology* **29**, 445–522.

Berman, R. G. (1990). Mixing properties of Ca–Mg–Fe–Mn garnets. *American Mineralogist* **75**, 328–344.

Bhattacharya, A., Mazumdar, A. C. & Sen, S. K. (1988). Fe–Mg mixing in cordierite: constraints from natural data and implications for cordierite–garnet geothermometry in granulites. *American Mineralogist* **73**, 338–344.

Bravo Espinosa, P. J. (2001). Geologia del borde oriental de la cordillera de la costa entre los rios Mataquito y Maule, VII región. B.Sc. thesis, Universidad de Chile, Santiago, 113 pp.

Brix, M. R., Stöckhert, B., Seidel, E., Theye, T., Thomson, S. N. & Küster, M. (2002). Thermobarometric data from a fossil zircon partial annealing zone in high pressure–low temperature rocks of eastern and central Crete, Greece. *Tectonophysics* **349**, 309–326.

Brown, T. H., Berman, R. G. & Perkins, E. H. (1989). Ge0-Calc: software package for calculation and display of pressure–temperature–composition phase diagrams using an IBM or compatible personal computer. *Computers and Geosciences* **14**, 279–289.

Dale, J., Holland, T. J. B. & Powell, R. (2000). Hornblende–garnet–plagioclase thermobarometry: a natural assemblage calibration of the thermodynamics of hornblende. *Contributions to Mineralogy and Petrology* **140**, 353–362.

De Capitani, C. & Brown, T. H. (1987). The computation of chemical equilibrium in complex systems containing non-ideal solid-solutions. *Geochimica et Cosmochimica Acta* **51**, 2639–2652.

Ernst, W. G. (1975). Systematics of large-scale tectonics and age progressions in Alpine and Circum-Pacific blueschist belts. *Tectonophysics* **26**, 229–246.

Evans, B. W. (1990). Phase relations of epidote-blueschists. *Lithos* **25**, 3–23.

Gana, P. & Hervé, F. (1983). Geologia del basamento cristalino en la Cordillera de la Costa entre los rios Mataquito y Maule, VII region. *Revista Geologica de Chile* **19–20**, 37–56.

Gerya, T. V., Maresch, W. V., Willner, A. P., Van Reenen, D. D. & Smit, C. A. (2001). Inherent gravitational instability of thickened continental crust with regionally developed low- to medium-pressure granulite facies metamorphism. *Earth and Planetary Science Letters* **190**, 221–235.

Gerya, T. V., Stöckhert, B. & Perchuk, A. L. (2003). Exhumation of high-pressure metamorphic rocks in a subduction channel—a numerical simulation. *Tectonics* **142**, 6-1–6-19.

Godoy, E. (1970). Estudio petrográfico del granito de Constitución y su aureola de metamorfismo de contacto. B.Sc. thesis, Universidad de Chile, Santiago, 130 pp.

Godoy, E. (1986). Die Entwicklung des Gondwana-Randes in Chile während des Paläozoikums unter besonderer Berücksichtigung der geotektonischen Stellung der Metavulkanite. Doct. thesis, University of Münster, 70 pp.

Godoy, E. & Kato, T. (1990). Late Paleozoic serpentinites and mafic schists from the Coast Range accretionary complex, Central Chile: their relation to aeromagnetic anomalies. *Geologische Rundschau* **79**, 121–130.

González Bonorino, F. (1971). Metamorphism of the crystalline basement of central Chile. *Journal of Petrology* **12**, 149–175.

Gutscher, M. A., Kukowski, N., Malavieille, J. & Lallemand, S. (1998). Material transfer in accretionary wedges from analysis of a systematic series of analog experiments. *Journal of Structural Geology* **20**, 407–416.

Graham, C. M. & Powell, R. (1984). A garnet–hornblende geothermometer and application to the Peloma Schist, southern California. *Journal of Metamorphic Geology* **2**, 13–32.

Hervé, F. (1988). Late Paleozoic subduction and accretion in Southern Chile. *Episodes* **11**, 183–188.

Hervé, F., Munizaga, F., Parada, M. A., Brook, M., Pankhurst, R. J., Snelling, N. J. & Drake, R. (1988). Granitoids of the coast range of central Chile: geochronology and geologic setting. *Journal of South American Earth Sciences* **1**, 185–194.

Holland, T. J. B. (1980). The reaction albite = jadeite + quartz determined experimentally in the range 600–1200°C. *American Mineralogist* **65**, 129–134.

Holland, T. J. B. & Powell, R. (1998a). An internally consistent thermodynamic data set for phases of petrological interest. *Journal of Metamorphic Geology* **16**, 309–343.

Holland, T. J. B. & Powell, R. (1998b). Mixing properties and activity–composition relationships of chlorites in the system MgO–FeO–Al$_2$O$_3$–SiO$_2$–H$_2$O. *European Journal of Mineralogy* **10**, 395–406.

Johannes, W. (1984). Beginning of melting in the granite system Qz–Or–Ab–An–H$_2$O. *Contributions to Mineralogy and Petrology* **86**, 264–273.

Kato, T. T. (1985). Pre-Andean orogenesis in the Coast Ranges of Central Chile. *Geological Society of America Bulletin* **96**, 918–924.

Kretz, R. (1983). Symbols for rock-forming minerals. *American Mineralogist* **68**, 277–279.

Kukowski, N., Lallemand, S. E., Malavieille, J., Gutscher, M. A. & Reston, T. J. (2002). Mechanical decoupling and basal duplex formation observed in sandbox experiments with application to the Western Mediterranean Ridge accretionary complex. *Marine Geology* **186**, 29–42.

Leake, B. E., Woolley, A. R., Arps, C. E. S., *et al.* (1997). Nomenclature of amphiboles. Report of the subcommittee on amphiboles of International Mineralogical Association Committee on New Minerals and Mineral Names. *European Journal of Mineralogy* **9**, 623–651.

Leterrier, J., Maury, R., Thonon, P., Girard, D. & Marchal, M. (1982). Clinopyroxene composition as a method of identification of magmatic affinities of paleovolcanic series. *Earth and Planetary Science Letters* **59**, 139–154.

Lucassen, F., Trumbull, R., Franz, G., Creixell, C., Vásquez, P., Romer, R. L. & Figueroa, O. (2004). Distinguishing crustal recycling and juvenile additions at active continental margins: the Paleozoic to recent compositional evolution of the Chilean continental margin (36°–41°S). *Journal of South American Earth Science* **17**, 103–119.

Martin, M. W., Kato, T. T., Rodriguez, C., Godoy, E., Duhart, P., McDonough, M. & Campos, A. (1999). Evolution of the late Paleozoic accretionary complex and overlying forearc–magmatic arc, south central Chile (38°–41°S): constraints for the tectonic setting along the southwestern margin of Gondwana. *Tectonics* **18**, 582–605.

Massonne, H.-J. (1995a). *P–T* evolution of metavolcanics from the southern Taunus mountains. In: Dallmeyer, R. D., Franke, W. & Weber, K. (eds) *Pre-Permian Geology of Central and Eastern Europe*. Berlin: Springer, pp. 132–137.

Massonne, H.-J. (1995b). Experimental and petrogenetic study of UHPM. In: Coleman, R. G. & Wang, X. (eds) *Ultrahigh Pressure Metamorphism*. Cambridge: Cambridge University Press, pp. 33–95.

Massonne, H.-J. (1997). An improved thermodynamic solid solution model for natural white micas and its application to the geothermobarometry of metamorphic rocks. *Mineral Equilibria and Databases, Abstracts. Geological Survey of Finland, Guide* **46**, 49.

Massonne, H.-J. & Schreyer, W. (1986). High-pressure syntheses and X-ray properties of white micas in the system K$_2$O–MgO–Al$_2$O$_3$–SiO$_2$–H$_2$O. *Neues Jahrbuch für Mineralogie, Abhandlungen* **153**, 177–215.

Massonne, H.-J. & Szpurka, Z. (1997). Thermodynamic properties of white micas on the basis of high-pressure experiments in the systems K$_2$O–MgO–Al$_2$O$_3$–SiO$_2$–H$_2$O and K$_2$O–FeO–Al$_2$O$_3$–SiO$_2$–H$_2$O. *Lithos* **41**, 229–250.

McMullin, D. W., Berman, R. G. & Greenwood, H. J. (1991). Calibration of the SGAM thermometer for pelitic rocks using data from equilibrium experiments and natural assemblages. *Canadian Mineralogist* **29**, 889–908.

Moraga, J. (1981). Geología de la Cordillera de la Costa entre Punta Sirena y el Rio mataquito. B.Sc. thesis, Universidad de Chile, Santiago.

Nisbet, E. G. & Pearce, J. A. (1977). Clinopyroxene composition in mafic lavas from different tectonic settings. *Contributions to Mineralogy and Petrology* **63**, 149–160.

Parra, T., Vidal, O. & Jolivet, L. (2002*a*). Relation between the intensity of deformation and retrogression in blueschist metapelites of Tinos Island (Greece) evidenced by chlorite–mica local equilibria. *Lithos* **63**, 41–66.

Parra, T., Vidal, O. & Agard, P. (2002*b*). A thermodynamic model for Fe–Mg dioctahedral K-white micas using data from phase equilibrium experiments and natural pelitic assemblages. *Contributions to Mineralogy and Petrology* **143**, 706–732.

Peacock, S. M. (1996). Thermal and petrologic structure of subduction zones. In: Behout, G. E., Scholl, D. W., Kirby, S. H. & Platt, J. (eds) *Subduction—Top to Bottom. Geophysical Monograph, American Geophysical Union* **96**, 119–131.

Powell, R. & Holland, T. J. B. (1999). Relating formulations of the thermodynamics of mineral solid solutions: activity modeling of pyroxenes, amphiboles and micas. *American Mineralogist* **84**, 1–14.

Spear, F. S. & Cheney, J. T. (1989). A petrogenetc grid for pelitic schists in the system SiO_2–Al_2O_3–FeO–MgO–K_2O–H_2O. *Contributions to Mineralogy and Petrology* **101**, 149–164.

Trouw, R. A. J., Simoes, L. S. A. & Valladares, C. S. (1998). Metamorphic evolution of a subduction complex, South Shetland Islands, Antarctica. *Journal of Metamorphic Geology* **16**, 475–490.

Vidal, O. & Parra, T. (2000). Exhumation paths of high-pressure metapelites obtained from local equilibria for chlorite–phengite assemblages. *Geological Journal* **35**, 139–161.

Vidal, O., Parra, T. & Trotet, F. (2001). A thermodynamic model for Fe–Mg aluminous chlorite using data from phase equilibrium experiments and natural pelitic assemblages in the 100–600°C, 1–25 kbar range. *American Journal of Science* **6**, 557–592.

Vinograd, V. L. (2002*a*). Thermodynamics of mixing and ordering in the diopside–jadeite system: I. A CVM model. *Mineralogical Magazine* **66**, 513–536.

Vinograd, V. L. (2002*b*). Thermodynamics of mixing and ordering in the diopside–jadeite system: II. A polynomial fit to the CVM results. *Mineralogical Magazine* **66**, 537–545.

Wakabayashi, J. (1990). Counterclockwise *PTt* paths from amphibolites, Franciscan Complex, California: relics from the early stages of subduction zone metamorphism. *Journal of Geology* **98**, 657–680.

Will, T., Okrusch, M., Schmädicke, E. & Chen, G. (1998). Phase relations in the greenschist–blueschist–amphibolite–eclogite facies in the system Na_2O–CaO–FeO–MgO–Al_2O_3–SiO_2–H_2O (NCFMASH), with application to metamorphic rocks from Samos, Greece. *Contributions to Mineralogy and Petrology* **132**, 85–102.

Willner, A. P., Hervé, F. & Massonne, H.-J. (2000). Mineral chemistry and pressure–temperature evolution of two contrasting high-pressure–low-temperature belts in the Chonos Archipelago, Southern Chile. *Journal of Petrology* **41**, 309–330.

Willner, A. P., Pawlig, S., Massonne, H.-J. & Hervé, F. (2001). Metamorphic evolution of spessartine quartzites (coticules) in the high pressure/low temperature complex at Bahia Mansa (Coastal Cordillera of Southern Central Chile). *Canadian Mineralogist* **39**, 1547–1569.

Willner, A. P., Hervé, F., Thomson, S. N. & Massonne, H.-J. (2004*a*). Converging *P–T* paths of Mesozoic HP–HT metamorphic units (Diego de Almagro Island, Southern Chile): evidence for juxtaposition during late shortening of an active continental margin. *Mineralogy and Petrology* **81**, 43–84.

Willner, A. P., Glodny, J., Gerya, T. V., Godoy, E. & Massonne, H.-J. (2004*b*). A counterclockwise *PT*-path of high pressure–low temperature rocks from the Coastal Cordillera accretionary complex of south–central Chile: constraints for the earliest stage of subduction mass flow. *Lithos* **75**, 283–310.

Willner, A. P., Thomson, S. N., Kröner, A., Wartho, J.-A., Wijbrans, J. R. & Hervé, F. (2005). Time markers for the evolution and exhumation history of a Late Palaeozoic paired metamorphic belt in north–central Chile (34°–35°30′S). *Journal of Petrology* **46**, 1835–1858.